Title
Formation of Anticyclones above Topographic Depressions

Journal
Journal of Physical Oceanography, 51(1)

ISSN
0022-3670

Authors
Solodoch, Aviv
Stewart, Andrew L
McWilliams, James C

Publication Date
2021

DOI
10.1175/jpo-d-20-0150.1

Formation of anticyclones above topographic depressions

Aviv Solodoch*, Andrew L. Stewart, and James C. McWilliams.

Dept. of Atmospheric and Oceanic Sciences, University of California, Los Angeles, California, USA

ABSTRACT

Long-lived anticyclonic eddies (ACs) have been repeatedly observed over several North Atlantic basins characterized by bowl-like topographic depressions. Motivated by these previous findings, the authors conduct numerical simulations of the spin-down of eddies initialized in idealized topographic bowls. In experiments with 1 or 2 isopycnal layers, it is found that a bowl-trapped AC is an emergent circulation pattern under a wide range of parameters. The trapped AC, often formed by repeated mergers of ACs over the bowl interior, is characterized by anomalously low potential vorticity (PV). Several PV segregation mechanisms that can contribute to the AC formation are examined. In one-layer experiments, the dynamics of the AC are largely determined by a nonlinearity parameter (ϵ) that quantifies the vorticity of the AC relative to the bowl's topographic PV gradient. The AC is trapped in the bowl for low $\epsilon \lesssim 1$, but for moderate values ($0.5 \lesssim \epsilon \lesssim 1$) partial PV segregation allows the AC to reside at finite distances from the center of the bowl. For higher $\epsilon \gtrsim 1$, eddies freely cross the topography and the AC is not confined to the bowl. These regimes are characterized across a suite of model experiments using ϵ and a PV homogenization parameter. Two-layer experiments show that the trapped AC can be top- or bottom-intensified, as determined by the domain-mean initial vertical energy distribution. These findings contrast with previous theories of mesoscale turbulence over topography that predict the formation of a prograde slope current, but do not predict a trapped AC.

1. Introduction

In several ocean basins, long-lived and semi-stationary mesoscale anticyclones (ACs) appear above topographic bowls[1]. Examples are the Mann Eddy (Mann 1967), Lofoten Basin Eddy (e.g., Ivanov and Korablev 1995; Köhl 2007; Søiland et al. 2016), and the Rockall Trough Eddy (Le Corre et al. 2019). The eddies have a clear climatological signature in sea-surface-height, as seen from satellite altimetry (figure 1). The first two have been repeatedly sampled in hydrographic surveys since their first discoveries. In the elongated bowl-like Iceland Basin long-lived ACs also appear to be common (Martin et al. 1998; Wade and Heywood 2001; Read and Pollard 2001; Zhao et al. 2018).

The aforementioned ACs all occur in mid to high latitude North Atlantic[2] seas or basins, where stratification is relatively weak, and the Coriolis parameter (f) is relatively high. This results in a larger tendency for currents to respond to seabed depth (H) variations (Salmon 1998) and follow ambient potential vorticity (f/H) contours (Isachsen et al. 2003). The latter are often well-approximated by H contours due to the limited relative f variation in higher latitudes compared with relative H variation across basins (Nøst and Isachsen 2003). Thus the effect of topographic depressions may be enhanced in these areas and play a role in the formation of the observed ACs.

Significant thermohaline fluxes and transformations occur in these basins, processes of climatic significance as part of the Atlantic Meridional Overturning Circulation (AMOC). It is still unclear whether the semi-stationary ACs impact these regional processes. Tulloch and Marshall (2012) have shown that AMOC variability is associated with a spatial pattern of density variability that peaks in the region of the Mann Eddy, in two ocean general circulation models. The Lofoten Basin Eddy attains anomalously large wintertime mixed layer depths (Yu et al. 2017). It encompasses a large reservoir of heat, absorbing warm eddies shed from poleward flowing boundary currents (Raj et al. 2015; Søiland et al. 2016). Richards and Straneo (2015) presented evidence for water mass transformation within a Lofoten Basin anticyclonic eddy.

Several different mechanisms have previously been suggested to sustain these eddies. Ivanov and Korablev (1995) suggested that wintertime intermediate-depth convection can regenerate the Lofoten Basin Eddy following a slow annual erosion. Köhl (2007) presented evidence that the Lofoten Basin Eddy is maintained by repeated mergers with ACs, which are shed from the Norwegian Atlantic Current and descend into the Lofoten Basin due to planetary and topographic beta drift (see Carnevale et al. 1991). The importance of eddy mergers vs convection in Lofoten Basin Eddy maintenance has also been discussed by (e.g.,

*Corresponding author: Aviv Solodoch, asolodoch@atmos.ucla.edu

[1]We loosely define a bowl as a topographic depression which has a central relatively flat region of similar width or wider than the outer slope region.

[2]The North Atlantic is by far the most-sampled of the oceans, and hence a statistical bias may be present.

Søiland and Rossby 2013; Raj et al. 2015; Volkov et al. 2015; Bashmachnikov et al. 2017; Bosse et al. 2019; Trodahl et al. 2020). Le Corre et al. (2019) showed that the Rockall Trough Eddy is similarly replenished by ACs, resulting from frictional vorticity generation at the adjacent topographic slope. Zhao et al. (2018) showed that Iceland Basin ACs are likely formed locally through mixed baroclinic-barotropic instability of the adjacent slope current. Rossby (1996) suggested that the Mann eddy is spawned from ACs released from the anticyclonic side of the adjacent North Atlantic Current.

In contrast, several theoretical and numerical studies have shown that in the absence of large scale external flow, mesoscale variability tends to produce rectified prograde[3] mean flows. That is, cyclonic (anticyclonic) circulation develops over topographic depressions (bumps), consistently with vorticity stretching (compression). This is predicted by "enstrophy-minimization" theory (Bretherton and Haidvogel 1976)[4], as well as statistical mechanics theories of topographic turbulence (starting with Salmon et al. 1976). This tendency is commonly known as the "Neptune" effect (e.g., Merryfield et al. 2001). With an imposed large scale impinging flow, dynamical seamount circulation theories also predict development of a prograde mean circulation over topographic anomalies seamount, i.e., a Taylor Cap (Hogg 1973; Huppert and Bryan 1976), as indeed had been observed in the ocean[5] (Hogg 1973; Owens and Hogg 1980; Richardson 1981; Freeland 1994; White and Mohn 2004). Alternative mechanisms must therefore explain the presence of long-lived ACs in topographic "bowls".

Although separate formation mechanisms were previously suggested for each of the above-mentioned semi-stationary oceanic ACs, there is not presently a unified dynamical understanding of AC formation and longevity above bowl-like topographic depressions. With the aim of achieving such an understanding, in this study we pose an idealized topographic-turbulence problem. Specifically, we conduct numerical simulations of the free evolution of mesoscale eddies randomly initialized over topographic depressions. We restrict our attention to the layered primitive equations, in one or two density layers, allowing wide sweeps of parameter space.

A description of the numerical experiments configurations is given in section 2. In section 3 we show that ACs form consistently over isolated topographic bowls in a very wide set of circumstances in single-layer experiments, and characterize the range of dynamical regimes that emerge in our simulations. In section 4 we investigate the degree of cross-topography exchange involved in AC formation, and its dynamical mechanisms. In section 5 we show that bowl ACs form from barotropic as well as baroclinic initial conditions in 2-layer experiments, and investigate the dependence of its final vertical structure on the initial conditions. A discussion and comparison with previous results is presented in section 6. A summary and conclusions are given in section 7.

[3]The same propagation direction as that of coastal Kelvin waves and topographic Rossby waves.

[4]Based on the tendency of enstrophy to dissipate faster than energy in 2d turbulence.

[5]Such circulations can also result from tidal rectification (e.g., Beckmann and Haidvogel 1997).

2. Methods

a. Layered Primitive Equations model

We conduct our simulations using the layered primitive equations model AWSIM (Stewart and Dellar 2016). A layered primitive equations model (McWilliams 2006) represents the simplest setting for studying topographic turbulence with finite amplitude topography and finite amplitude circulation effects. A primitive equation model is preferred over a quasi-geostrophic model because some of the observed ACs (section 1) have a high Rossby number ($\zeta = O(f)$) and reside in areas with $O(1)$ changes in H (Søiland et al. 2016; Yu et al. 2017; Le Corre et al. 2019).

The main model equations and its numerical scheme are described more fully in Stewart and Dellar (2016). Here we summarize salient aspects of the model. The dynamical equations are discretized via finite differences on an Arakawa C grid. The spatial discretization of the momentum and thickness equations (Stewart and Dellar 2016) is essentially identical to Arakawa and Lamb (1981) for the present experiments. Time stepping scheme follows the third-order Adams-Bashforth scheme (Durran 1991). The model conserves total energy, layer-wise potential enstrophy, and mass to machine precision in the absence of explicit dissipation (Stewart and Dellar 2016). A rigid upper lid condition is applied for computational efficiency, and surface pressure is diagnosed at each time step by numerical solution of the associated elliptic equation using a multi-grid method. Grid-scale accumulation of energy and enstrophy is controlled using a hyperviscous operator in the momentum equation (Griffies and Hallberg 2000).

The model can also evolve a passive tracer using an advection-diffusion equation, which was implemented in several of the experiments we conducted. We used the flux-limited tracer advection scheme of Kurganov and Tadmor (2000), which allows us to integrate the tracer equation without any explicit diffusion operator in the tracer advection equation.

b. Main experiments

We conduct most of our experiments using an isolated topographic bowl, with the following topographic depth (H) structure:

$$H = H_0 + \frac{H_b}{2}\left[1 - \tanh\left(\frac{r - R_b}{W_b}\right)\right]. \qquad (1)$$

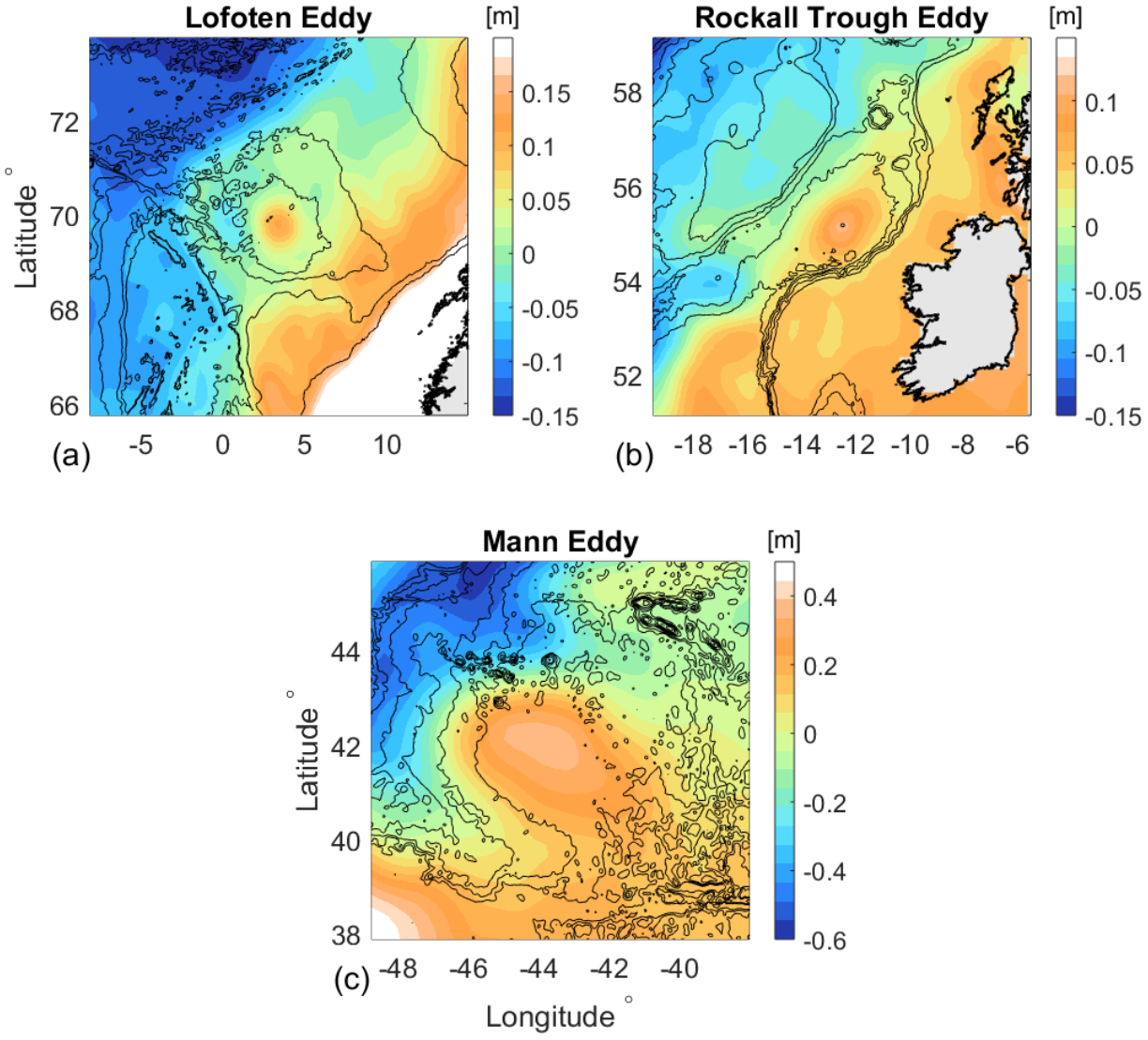

FIG. 1: Observed mean Sea Surface Height (SSH, in color, between 1993-2018) is shown at three ocean basins with bowl-like bathymetry and semi-permanent anticyclones within the bowls: (a) Lofoten Basin; (b) Rockall Trough; (c) Newfoundland Basin. The climatological (time-mean) locations of long-lived semi-stationary anticyclonic vortices (section 1) are identified by local maxima in SSH within the bowls in each panel. Daily SSH data ("Absolute Dynamics Topography") was obtained from the SEALEVEL_GLO_PHY_L4_REP_OBSERVATIONS_008_047 product distributed by Copernicus (https://marine.copernicus.eu/). A (dynamically irrelevant) constant value is subtracted from each panel for visual clarity. Colormaps in panels (a) and (c) are saturated at high (low) values in areas far from the relevant anticyclone. Bathymetry is shown in thin black contours denoting, in (a) [-3200,-3000:1000:-1000], (b) [-3000:500:-1000], (c) [-5000:500:-2000] m depth. Land is in gray: Norway and Ireland, in panels (a) and (b), respectively. Coastlines are marked by thick black lines. For maps of f/H contours, the reader is referred to Isachsen et al. (2003).

Here H_0 is depth far outside of the bowl, H_b is bowl depth relative to H_0, R_b is bowl radius, and r is distance from bowl center. We call W_b the slope half-width, since most of the topographic variation (76%) occurs over a distance

$\pm W_b$ from slope center, and since the slope decreases appreciably at larger distances. We are interested mostly in small W_b/R_b values, which prescribe relatively flat bowl interiors (section 1). For example, with $W_b/R_b = 1/6$, the slope magnitude at $r = R_b - W_b$ is already an order of magnitude smaller compared with at $r = R_b$. Examples of several H profiles with different parameter choices used in our experiments are shown in figure 2. Experiments with more complex topography are discussed in section 6.

The initial velocity field is prescribed randomly such that dominant length scales are smaller than bowl size (e.g., its radius). Initial conditions for velocity are defined by a velocity streamfunction ψ, i.e., $v = \partial_x\psi$, $u = -\partial_y\psi$. The streamfunction is defined by its discrete Fourier transform,

$$\hat{\psi}_{k,l} = N^{-1}K^{-1}e^{-((K-K_0)/dK)^2}e^{i\theta_k}. \qquad (2)$$

Here $K = \sqrt{k^2+l^2}$ is the magnitude of the wavenumber vector $k\hat{\boldsymbol{x}}+l\hat{\boldsymbol{y}}$, where $\hat{\boldsymbol{x}}$ and $\hat{\boldsymbol{y}}$ are unit vectors in the x and y directions, respectively. The dependence of the eddy energy on wavelength is set by K_0, the wavenumber at which the spectral power peaks, and $dK = K_0/8$, the exponential width of the spectral power maximum. The phase θ_k of each Fourier component (k,l) is randomly generated from a uniform $[0,2\pi]$ distribution. The factor N is a normalization constant that is selected to make domain-averaged kinetic energy density equal to a prescribed value E. An example of the resulting initial conditions is shown in figure 2a.

Table 1 lists our main single-layer experiments. We divide the experiments into batches according to the values of the geometric parameters H_0, H_b, R_b, W_b, and $\lambda_0 = 2\pi/K_0$. In each batch we fix these parameters and vary the initial kinetic energy density E. Each experiment is then referred to via the naming convention $BnEm$, where n is the batch number (left column of the corresponding row in table 1), and m is the experiment number within that batch. We set m equal to 1, 2, 3,... to denote the experiments with 1st, 2nd, 3rd,... lowest initial kinetic energies within each batch.

The values of H_0 used are typical of deep seas ($\sim$ 2 km) or abyssal ocean depths ($\sim$ 4 km). The values H_b = 0.1–0.5, R_b = 150–300, and W_b = 50–100 km, are loosely based on values relevant for the Mann eddy basin, although the latter is significantly more complicated than a symmetric bowl shape. The selected kinetic energy density values span (and surpass a factor of $\sim$ 2) the range of typical ocean velocities, i.e., velocity scales of cm/s to several m/s. We set the Coriolis parameter to a value of $f = 10^{-4}\ s^{-1}$ in all cases.

Unless otherwise specified, we conduct our experiments in square domain with a side length of 1000 km. We use periodic boundary conditions to facilitate comparison with topographic turbulence theories. We conducted several experiments with wall boundary conditions or with periodic domains multiple times larger, but we found no appreciable differences in the resulting bowl circulation. The horizontal resolution (dx) used is uniform and is either $\approx$ 2 or 1 km, corresponding to 512^2 or 1024^2 grid cells, respectively. The latter was used only in batch 1. In all cases $dx \le \lambda_0/46$. We re-ran various experiments from several different batches with the grid spacing decreased by a factor of 2-4 to check the resolution sensitivity, but these experiments exhibited little quantitative and qualitative differences. Biharmonic momentum dissipation with constant coefficient $A_4 = 0.01dx^3U_0$ was used, where $U_0 = 1.5\ \max|\boldsymbol{u_0}(\boldsymbol{x})|$, and $\boldsymbol{u_0}(\boldsymbol{x})$ is the initial fluid velocity at position $\boldsymbol{x}$. Re-running several experiments with Smagorinsky-like (Griffies and Hallberg 2000) biharmonic dissipation operator instead resulted in negligible quantitative differences. We also verified that kinetic energy does not accumulate at the grid scale over time — a sign of insufficient grid-scale dissipation. Minimal experiment duration was 500 days. Model output was saved in 5-day (1-day) averages in batches 1-5 (6-9), except where noted otherwise.

A tracer field (section 2a) is implemented in all experiments of batches 2, 3, and 6. We set the tracer initial condition $c(x,y,t=0) = c_0(r)$, where r is distance from bowl center, as follows:

$$c_0(r) = \left[1 - \tanh\left(\frac{r - R_b - W_b}{W_c}\right)\right]/2. \qquad (3)$$

This prescription is advantageous in estimating total cross-slope material transport (see section 4). The parameter W_c is set to a value of 10 km to minimize the width of the transition in the tracer concentration without introducing numerical artifacts in the calculation.

c. Coherent monopole and dipole experiments

To investigate dynamics of isolated vortices in the bowl geometry, we also conducted several experiments with a different circulation initialization scheme (results reported in section 4). Instead of random and domain-filling disturbances, either a single coherent anticyclone (monopole) or an AC-cyclone pair (dipole) was initialized outside of the bowl. The topographic parameters used were $H_0 = 4$, $R_b = 300$, $W_b = 50$, and $H_b = 0.5\ km$. A domain length of 1500–2000 km was used, with little difference between the two, and with 1024^2 grid cells. All other parameters were identical to those described above. The prescription of a single vortex (centered at initial location $\underline{x}_0$) was by a Gaussian streamfunction with length scale r_0 [m^{-1}]:

$$\psi(\underline{x}) \sim \exp\left(\frac{-(\underline{x}-\underline{x}_0)^2}{2r_0^2}\right) \qquad (4)$$

A dipole was created by superposing two eddies of the form (4) with opposing signs.

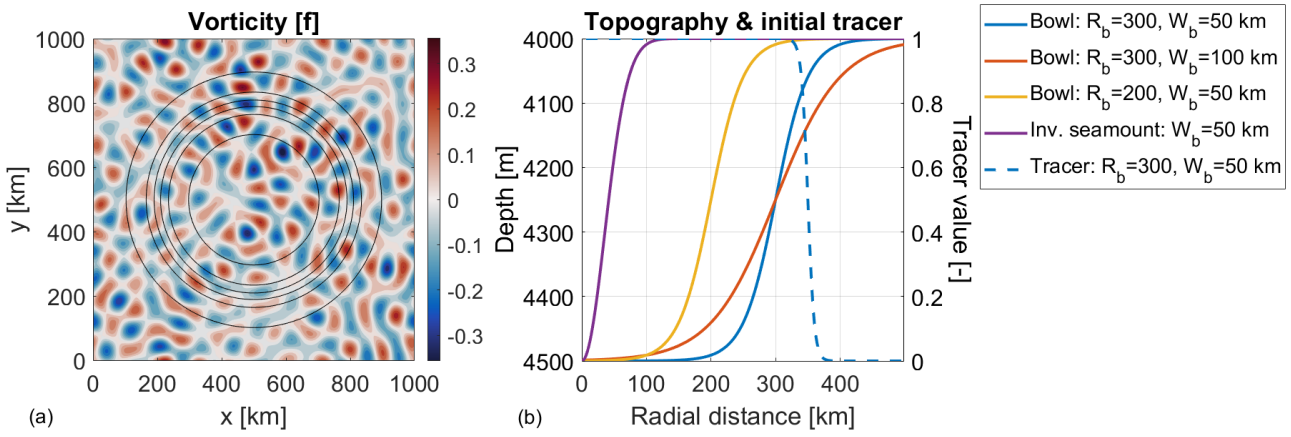

FIG. 2: Initial conditions and examples of the experimental bathymetry. (a) Example of randomly generated vorticity initial conditions (in units of the Coriolis parameter f), with mean kinetic energy $E = 0.01$ [m^2/s^2] and dominant wavelength $\lambda_0 = 90$ km. Black contours show the (4010,4100,4200,4300,4400,4490) [m] isobaths, for topographic parameters $R_b = 300$, $W_b = 50$, $H = 4$, $H_b = 0.5$ km (section 2b). This domain geometry is typical of experiments described in sections 3-5. In panel (b) solid curves (left axis values) show several examples of radial topographic "bowl" profiles used in our experiments. We define a "bowl" loosely as a depression with a slope region of width ($\sim 2W_b$) that is narrow relative to mid-slope radius (R_b). Bowl-like topographies are typical of the locations in which persistent ACs occur in the ocean (section 1). A single example of inverted seamount type topography is shown as well (in purple), in reference to the discussion in section 6. The right axis shows initial conditions for the passive tracer (equation 3). The tracer was included in experiment batches 2, 3, and 6 (see table 1).

TABLE 1: Summary of our main single-layer experiments. Each experiment is later referred to by a name of form: $BnEm$, where n is the batch number (left column of appropriate row in the table), and m is the experiment number within the same batch. Parameters pertaining to the topography and initial conditions (IC) are given in each column. An experiment number m of 1, 2, 3,... corresponds to the 1st, 2nd, 3rd,... lowest initial kinetic energy experiment within each batch (rightmost column). For example, experiment $B1E5$ (for which diagnostics are shown in figures 3-4) refers to the fifth lowest initial energy (0.05 m^2/s^2) among the experiments in the first row ($n = 1$).

Batch $B\#$	Bowl radius R_b [km]	External depth H_0 [km]	Depth change H_b [km]	Bowl half-width W_b [km]	IC: dominant wavelength λ_0 [km]	IC: average energy density E [m^2/s^2]
B1	300	4	0.5	50	45	0.001,0.005,0.01,0.02,0.05,0.1,0.2,0.5,1
B2	300	4	0.5	50	90	0.001,0.005,0.01,0.02,0.05,0.1,0.2,0.5,1,2
B3	300	4	0.1	50	90	0.001,0.005,0.01,0.02,0.05,0.1,0.2,0.5,1,2
B4	300	4	0.5	100	90	0.001,0.005,0.01,0.02,0.05,0.1,0.2,0.5,1,5
B5	150	4	0.5	50	90	0.001,0.005,0.01,0.02,0.05,0.1,0.2,0.5
B6	300	4	0.5	50	180	0.001,0.005,0.01,0.02,0.05,0.1,0.2,0.5
B7	300	2	0.5	50	180	0.001,0.005,0.01,0.02,0.05,0.1,0.2,0.5,1,5
B8	300	2	0.2	50	180	0.001,0.005,0.01,0.02,0.05,0.1,0.2,0.5
B9	200	2	0.5	50	180	0.001,0.005,0.01,0.05,0.1,0.2,0.3,0.4,0.6

d. Eddy Detection

To track the central AC we use an algorithm based on an Okubo-Weiss parameter (OWP) threshold. The OWP is defined by OWP $= s^2 - \zeta^2$, where s is horizontal strain ($s^2 = (u_x - v_y)^2 + (u_y + v_x)^2$), and $\zeta = v_x - u_y$ is the vorticity within an isopycnal layer. Eddies are characterized by negative OWP values, i.e., vorticity dominating over strain. Within a single time sample and isopycnal layer, a grid cell (with index i) is identified as a vortex-core candidate if the OWP in that cell satisfies $\mathrm{OWP}_i < -a\,\mathrm{STD}_{\mathrm{OWP}}$, where $\mathrm{STD}_{\mathrm{OWP}}$ is the spatial standard deviation of OWP for the same time sample and isopycnal layer, and a is a constant factor. Drawing on previous studies (Pasquero

et al. 2001; Isern-Fontanet et al. 2006; Volkov et al. 2015), we set $a = 0.2$.

A connected region of model grid cells is identified as containing a vortex "core" if each cell was identified as a candidate, if ζ is singly-signed in the connected region, and if the total area A is larger than an imposed minimum $\pi r_{\min}^2$. We choose $r_{\min} = 10$ km, equivalent to 5 grid cells for the lowest resolution experiments reported here. The detected eddy radius is defined as $r_e = \sqrt{A/\pi}$, where A is the detected (connected) area size. The detected eddy vorticity is defined as the spatially averaged vorticity within the detected area. In simulations that develop a bowl-trapped AC, we found that the AC could be tracked accurately by searching for the strongest AC within the bowl at any given time.

3. Emergence of barotropic bowl-trapped anticyclones

We begin by describing the results of a representative single 1-layer experiment in some detail, in subsection a. In subsection b we consider the results of all standard 1-layer experiments (section 2b and table 1) and identify nondimensional parameters that approximately constrain the properties of the bowl-trapped AC. In subsection c we investigate the long-time fate and stability of the emergent bowl AC. In subsection d, we present a vorticity budget for the evolution of the trapped AC and of the bowl slope current.

a. Emergent circulation over a bowl — case study

In this subsection we describe the results of experiment $B1E5$ (table 1), as an illustrative and typical example of bowl AC formation and of its properties in our experiments. The results of free evolution from the random initial conditions (section 2) are graphically summarized in figures 3,4, and a movie (SA1, supp. mat.).

Two main circulation patterns emerge within the bowl. One is a cyclonic slope-current, i.e., propagating with shallower water to its right (cyclonic in the present case). It is associated with positive vorticity in the inner slope region and somewhat interior to it, and azimuthal velocity peak at mid-slope. The second emergent circulation pattern is a central (bowl-trapped) AC. The AC is apparent by its negative vorticity around the bowl center (figure 3), and by its negative (retrograde) azimuthal velocity, peaking at a radius of about 60 km (figure 4a). Multiple (mainly cyclonic) eddies survive outside of the bowl (panel d), although in time they tend to merge into a smaller number (see movie SA1).

The emergence and intensification of the trapped AC is related to repeated merging of ACs (figure 3). Down-slope migration of ACs contributes to these mergers. In contrast, cyclones are cleared from the center of the bowl, leaving a diffuse cyclonic layer over most of the bowl interior, up to the center of the slope (figure 3d). A consequence of this redistribution of cyclonic and AC vorticity is that potential vorticity (PV) becomes segregated, with low PV material forming the center AC (figure 4b). Material transport and vortex cross-slope propagation are further investigated in subsection 4.

The emergence of a prograde slope current is to be expected based on topographic turbulence theories posed by previous studies (section 1), whereas the emergence of a central AC is not. This is underlined by the late-time streamfunction-PV relation (figure 4); this relation is multi-valued, contrary to the predictions of topographic turbulence theories (*e.g.* Bretherton and Haidvogel 1976). This point and further comparison with topographic turbulence theories are discussed in section 6. However, the evolution time scales of the slope current and of the AC are similar (figure 4a), which motivates a discussion of the relation between vorticity fluxes contributing to the AC and to the slope current formation (section 3d). The anticyclone is stable and long lived, in the sense that it is little-changed in form or amplitude from its formation, around day 150, until the end of the present experiment, at day 1000. The same applies to the slope current. AC longevity is further investigated in subsection c.

b. Regime diagram

(i) Non-linearity parameter. In this subsection we consider the conditions for bowl-trapped anticyclone formation across our entire array of experiments (table 1). We find that the formation or absence of a trapped AC is largely predicted by the value of a nonlinearity parameter. The parameter (ϵ) is defined by a vorticity magnitude V/L relative to fH_b/H_0, the value of topographically induced vorticity due to hypothetical crossing of the bowl slope:

$$\epsilon \equiv \frac{VH_0}{fH_bL}. \tag{5}$$

Here $V = \sqrt{2E}$ is the velocity scale, and L is an eddy length scale. The late-time radii of eddies (within and outside of the bowl) are of order 50 km in all cases, despite starting from different initial length scales. That is partially since topography limits the progression of the inverse cascade. Hence we set $L = 50$ km. The choice is preferable to using the final AC radius r_e since L (like V) is a "coarse-grained" parameter. However, we find that both choices result in similar ϵ values.

In figure 5a we plot the distance (D) of the AC from the center of the bowl (section 2d), averaged over the last 100 days of each experiment. This shows that trapped ACs form within the bowl in all instances with small enough ϵ, i.e., $\epsilon \lesssim 0.5$, and in most cases with $\epsilon = 0.5 - 1$. However, advection is necessary to the formation, i.e., no mean anticyclonic flow emerges inside the bowl in the limit $\epsilon \to 0$,

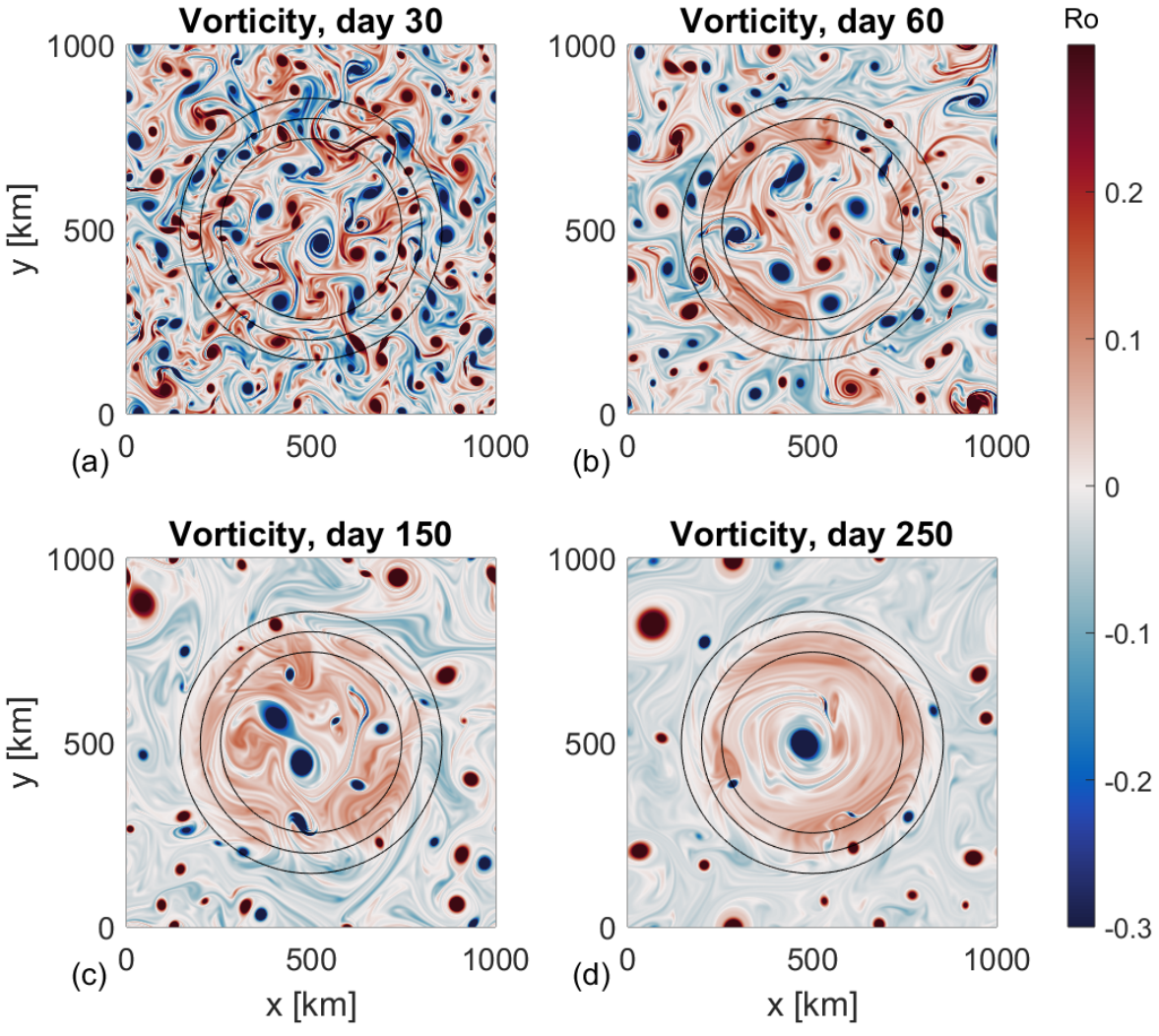

FIG. 3: Evolution over time and formation of a bowl-trapped anticyclone in experiment $B1E5$ (table 1). The instantaneous vorticity (in f units) distribution is shown at times indicated above each panel. Anticyclones aggregate within the bowl and repeatedly merge with each other, forming a long-lived AC confined to the central portion of the bowl. A cyclonic slope current also emerges, centered on the topographic slope, as seen by the broad regions of positive and negative vorticity inside and outside of the bowl, respectively. Note that the colormap is saturated to make the spatial features clearer. The 99th percentile vorticity magnitude is $0.78f$ and $0.42f$ in panels a and d, respectively. Black contours show the (4050,4250,4450) $[m]$ isobaths.

and neither does the slope current. In appendix B we verify this using a linear simulation. This is also consistent with the bowl vorticity budget (section 3d).

Significant variation in D occurs in the range $\epsilon = 0.5-1$, as discussed in (ii) below. At higher values of $\epsilon \gtrsim 1$ there is a transition to a regime with no bowl-trapped AC. In this regime, coherent eddies of both polarities freely move across the topography, their motions dominated by eddy-eddy interactions. Thus ϵ may be interpreted as determining the dominance of eddy-eddy vs eddy-topography effects. However, the cross-over does not occur sharply at a single ϵ value across different experiment batches, as there is substantial scatter in the diagnostics due to inter-experiment variations in the random initialization. Note that the slope current, predicted by topographic turbulence theories (section 1), persists in all cases.

Finally, we quantify the bowl-trapped AC strength, i.e., integrated vorticity in its core, $\Gamma \approx \zeta_0 \pi r_e^2$, were r_e is the di-

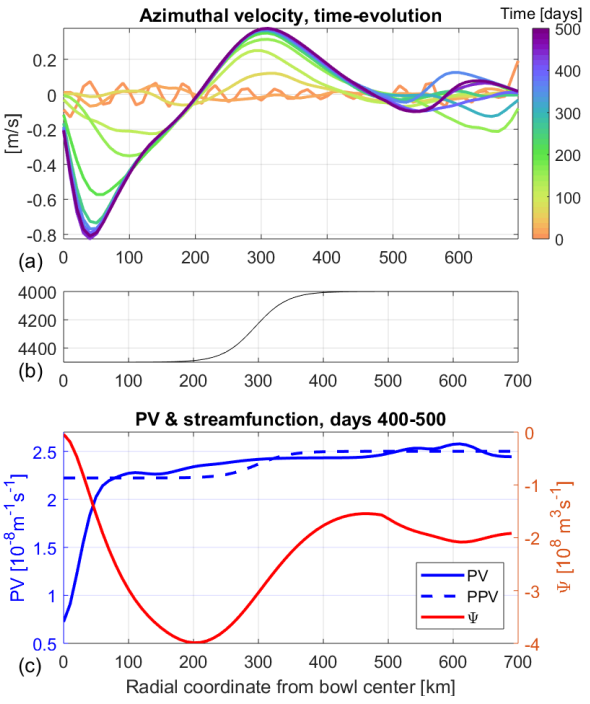

FIG. 4: Evolution and late time properties of the bowl-trapped anticyclone and of the slope-current in experiment $B1E5$ (table 1, figure 3). Displayed variables are averaged azimuthally in radial bins from the center of the bowl. (a) Azimuthal velocity evolution, in 50-day time-averages centered around days 25:50:500. The initial conditions are also shown for comparison, and times are indicated by line colors. (b) Bathymetric profile $H(r)$. (c) Late-time (days 400–500) time- and azimuthal-mean potential vorticity PV = $(f+\zeta)/H$, "Planetary" Potential Vorticity PPV = f/H, and transport streamfunction Ψ.

agnosed AC radius (section 2d). We pose a scaling for the core-averaged vorticity: $\zeta_0 \sim V_e/r_e$. Anticipating that V_e should scale with initial kinetic energy (E), we then pose $\Gamma = a\sqrt{E}\pi r_e$. We diagnose the value of the coefficient a in all experiments where a bowl trapped AC occurs. The result (mean ± standard deviation) is $a = -3 \pm 1$ across three orders of magnitude of E. Thus the AC is anomalously strong relative to scaling with domain-mean kinetic energy value, i.e., $|a|$ is ≥ 1. That is consistent with the accumulation of anomalously low PV within the AC through repeated mergers (section 3a).

(ii) Background PV homogenization For $\epsilon \sim 0.5-1$, the trapped AC typically drifts azimuthally around the bowl center, at a radius which tends to increase with ϵ. These states can occur even with AC close to the slope peak ($r = R_b$). We find that these AC states near the topographic slope occur in cases where "background" PV is homogenized within the bowl. "Background" here refers to the area outside of (excluding) the trapped AC, as defined by a PV inhomogeneity parameter below. The topographic beta-drift tendency, including in the cross-slope direction (Carnevale et al. 1991), is negated due to the homogenization of background PV. An illustrative example (experiment $B6E7$) is shown in figure 6. The particular experiment was chosen for visual clarity since PV homogenization is almost complete and the eddy drifts quite close to the slope center, but is otherwise typical of this regime.

In the quasigeostrophic (QG) approximation, vortices within jets with homogenized PV propagate with the local-mean (eddy PV-weighted) velocity (Marcus 1990). We show in appendix A that in Shallow Water Equations (SWE) there is an additional along-topography drift, not present in the QG approximation. This additional drift is related to topographic stretching of relative vorticity, and does not vanish with homogenized background PV. In the experiment $B6E7$ shown in figure 6, the AC drifts with propagation speed ~0.82 m/s. Calculation of the vortex propagation speed formula (A5) in appendix A gives in this case a theoretical drift speed of 0.9–1 m/s, of which 0.24–0.34 are due to the additional SWE term (relative vorticity stretching), and the remainder is due to vortex advection by the mean velocity. The $10-20\%$ deviation is potentially due to vortex effects on the slope current which advects it, since the vortex is of significant magnitude and since rigid-lid barotropic vortices have long-range velocity tails (McWilliams 2006).

The vortex in $B6E7$ is long-lived despite residing in a region of azimuthal-mean strain induced by the slope current. It was found by Marcus (1990) that a vortex can be stable within a large scale mean current $v(r)$ (flowing in the azimuthal direction, and varying in the radial direction) when its vorticity ζ has the same sign as the large-scale current radial strain, i.e., $\sigma = r\partial_r(v/r)$, and if σ/ζ is of $O(1)$ magnitude or smaller. Indeed in the present case ($B6E7$) the mean radial strain is about (-0.04) $[f]$ in the radial position of the AC, while AC vorticity $\approx -0.5f$, fulfilling both the sign and magnitude requirements of Marcus (1990). This implies that bowl-trapped ACs should be able to reside (while moving azimuthally) at any bowl radial position D within the homogenized area at which the mean strain is sufficiently small, i.e., a continuum (in D) of stable steady states (or limit cycles, to be precise) is available. Multiple different steady states were indeed found when repeating, e.g., experiment B6E7 several times with different random choices of initial phases (θ_k, section 2b) in each repeat experiment. The trapped AC radial position D (averaged over the last 100 days, as before) has a high relative variation between these (six) repeat experiments of B6E7, with a (cross-experiment) mean and standard

deviation $D/R_b = 0.55 \pm 0.25$[6]. Such repeat-experiments were conducted for all batch 6 (B6) experiments. Similarly to the repeats of experiment B6E7 (not shown), large variations in D/R_b at constant ϵ are found to be the rule for $0.5 < \epsilon < 1$, but are several times smaller for $\epsilon < 0.5$. The (partial) PV homogenization thus explains the possibility for trapped AC states at larger D/R_b values at $0.5 < \epsilon < 1$ (compared with smaller ϵ), and possibly also explains the substantial scatter in D/R_b over the same ϵ range in figure 5a.

Therefore, we now quantify background PV homogenization across our suite of experiments by defining a background PV inhomogeneity parameter,

$$\mathrm{PVI} = \frac{\text{PV IQR}}{\text{PPV IQR}}. \tag{6}$$

Here PV IQR is the PV inter-quartile range (IQR, the difference between 75th and 25th percentiles) within the bowl ($r < R_b$), excluding the trapped AC core, and PPV IQR is the IQR of the "planetary PV", PPV = f/H, in the same area. For partially or fully homogenized background PV cases, PVI < 1. Complete homogenization results in PVI = 0. We plot PVI against ϵ and against D in figure 5 panels b and c, respectively. As expected, we find that PVI decreases as ϵ increases, and in most cases approaches zero for $\epsilon \gtrsim 1$. Much of the scatter in D occurs when PVI ≤ 0.2. As discussed above, PV homogenization results in a multiplicity of possible "steady states" (limit cycles) that produces the scatter in the ϵ–D and PVI–D relations, visible in figure 5.

c. Long-term evolution

Here we explore the long term evolution of bowl-trapped ACs in our experiments. This is motivated by the persistence of ocean ACs over depressions (section 1), and also in comparison with topographic turbulence theories (section 6). In all experiments in which a bowl AC formed (deduced by its persistence for $\gtrsim 100$ days), it lasted for the rest of the experiment duration, with little qualitative or quantitative change. We also extended the duration of multiple experiments to several thousand days after AC formation, with similar results.

To further diagnose long term evolution of the bowl-trapped AC and its dynamical causes, we re-ran experiment $B1E3$ (hereby $B1E3L$) for 5000 days, with daily-mean outputs including online momentum equation diagnostics. The experiment develops a trapped AC close to the bowl center, as in experiment B1E5 discussed in section 3a. The spatial resolution was ~2 km, twice as coarse as experiment $B1E3$. Although the trapped AC core circulation at, e.g., day 500 is 25% higher in the higher-resolution experiment, the end states are qualitatively similar and well resolved in each simulation. Thus the coarser simulation diagnostics are informative about the late time evolution of the trapped AC.

The evolution of the $B1E3L$ AC between days 500 and 5000 is illustrated in figure 7. The AC central (peak) vorticity decays over time, by ~50%. However, the integrated circulation of the contiguous patch of negative-vorticity around the AC center does not change by more than 1%. The lack of appreciable circulation decay is not inconsistent with the peak vorticity decay, as the AC becomes wider with time (figure 7 panels a-b). The integrated circulation in the core region, as defined in section 2d, actually grows by 40% during this period[7].

We also diagnose the AC circulation evolution in an Eulerian frame. We calculate the circulation tendency at each time step due to each term in the momentum equation. We perform this analysis around the perimeter of a 50 km × 50 km square in the center of the bowl, which encloses the AC core. The perimeter is aligned with grid axes, to avoid introducing discretization errors. In figure 7c we show the circulation tendency due to the sum of the inviscid terms (nonzero contributions are due to advective terms) vs that due to the viscous term. As expected, the AC is initially spun-up by the inviscid terms. Similar to the Lagrangian analysis of the eddy core discussed above, this Eulerian analysis shows no clear decay in AC circulation after its formation. Circulation oscillations are of order 2%. The viscous term cause a slight $\approx 2\%$ decay in circulation between days 500 and 5000. We found that doubling the size of the perimeter used for this calculation did not qualitatively change the result. Therefore the AC does not decay directly by inviscid terms in a symmetric bowl, within at least a scale of thousands of days. The implications of these results are discussed in section 6.

d. Spin-up of the anticyclone and slope current: a vorticity budget

Here we show that the spin-up of the bowl anticyclone necessarily implies a tendency for cyclonic vorticity accumulation between the anticyclone and the topographic slope. We further suggest a scaling relation for determining the relative circulation magnitudes of the bowl anticyclone and of the slope current *a priori*.

We first derive an equation for the circulation tendency along an isobath by integrating the vorticity equa-

[6] In all of the B6E7 repeat experiments PV homogenization was near-complete, i.e., the metric PVI defined in the next paragraph was < 0.07. Compare with figure 5b-c.

[7] We do not attempt to determine here if this apparent intensification is an artifact of our definition of the core. For example the dying out of external transients may cause a larger area around the AC to be identified as part of the core.

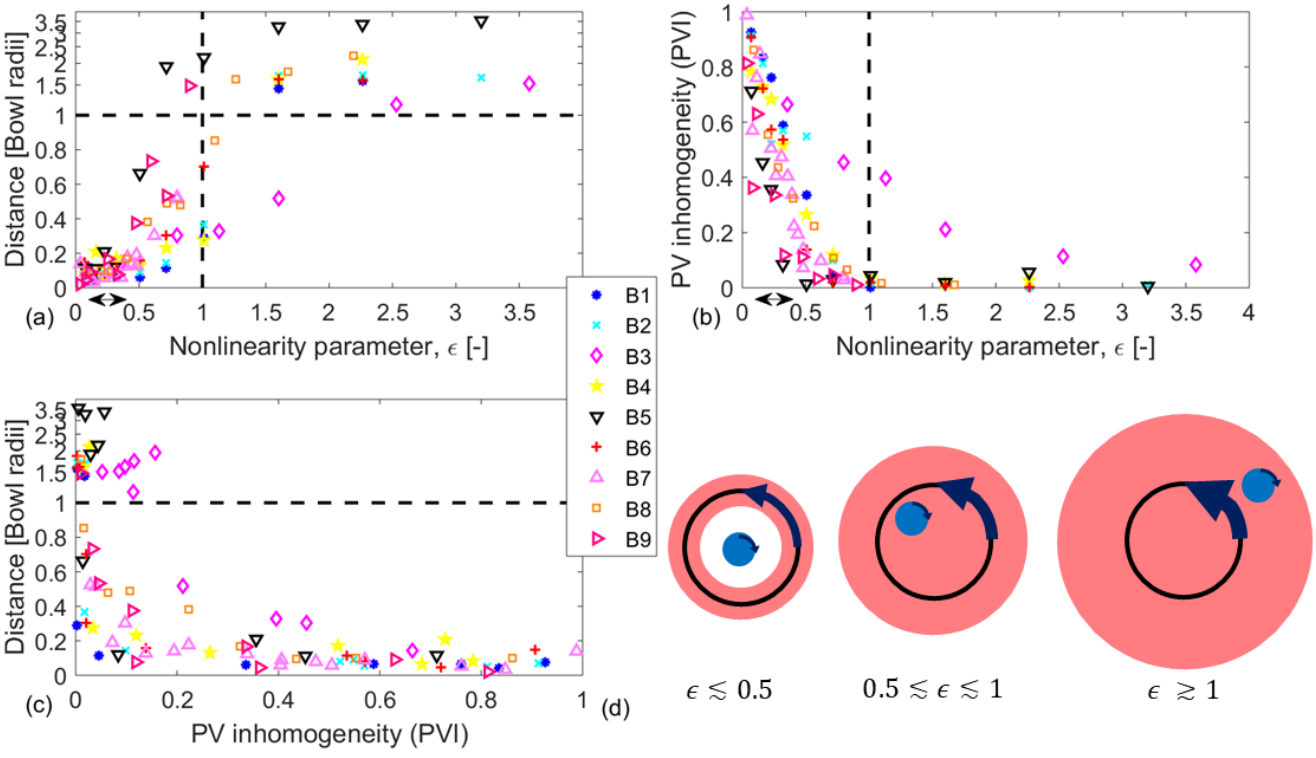

FIG. 5: Regime diagrams for bowl-trapped anticyclone (AC) formation (section 3b). (a) Mean normalized radial position (D/R_b) of the emergent anticyclone within the bowl for each free evolution experiment, versus the nonlinearity parameter $\epsilon \equiv VH/fH_bL$. The radial position r is normalized by bowl radius R_b. Bowl-trapped ACs correspond to $D/R_b < 1$. Values $D/R_b > 1$ are indicative of eddies (including ACs) moving freely across the bathymetry. (b) Position versus the PV inhomogeneity parameter (PVI, equation 6). (c) PVI vs ϵ. Each different colored marker represents a separate batch of experiments. Within each batch all parameters are kept identical except for the initialization energy E (section 2b). The D/R_b-axis scale is linear (logarithmic) for values below (above) 1. The dashed lines at $\epsilon = 1$ and at $D/R_b = 1$ serve as visual aids. In panels (a–b), the double-arrow shows the range of ϵ values estimated to be relevant for the Mann, Lofoten, and Rockall Trough eddies. (d) A schematic illustration of the three regimes described in panels a–c. Note that the states shown are typical but not unique for each regime. For low ϵ, a trapped AC emerges close to bowl center. For intermediate ϵ values, a bowl-trapped AC typically emerges, but can occur at some finite bowl-radius, since the intensified slope current (arrow) causes partial or complete PV homogenization (illustrated in red) within the bowl and outside of the AC. For high ϵ, the eddies are free to move across the slope and are not trapped within the bowl.

tion within the area bounded by that isobath:

$$\partial_t C(r,t) = \partial_t \int_0^{2\pi}\int_0^{r} \zeta \,\mathrm{d}A = -I(r,t) + \mathcal{F}, \qquad (7a)$$

$$I(r,t) = \int_{\phi=0}^{2\pi} \zeta'(r,\phi)u'(r,\phi)r\,\mathrm{d}\phi. \qquad (7b)$$

Here r denotes the distance from bowl center is denoted by r, u denotes the radial velocity, $\mathcal{F}$ denotes viscous terms, and primes denote deviations from an azimuthal average. In section 3c we showed that the primary contribution to circulation tendency is $I(r,t)$, i.e., cross-bathymetry eddy vorticity flux. Thus we hereafter neglect the viscous terms in (7a).

To address AC and slope current circulations, we define r_{AC} as the radial position of maximal magnitude in retrograde (anticyclonic) final-state azimuthal-mean velocity within the bowl. Likewise, we choose r_{SC} as the radial position of maximal magnitude in prograde (cyclonic) final-state azimuthal-mean velocity over the topographic slope.

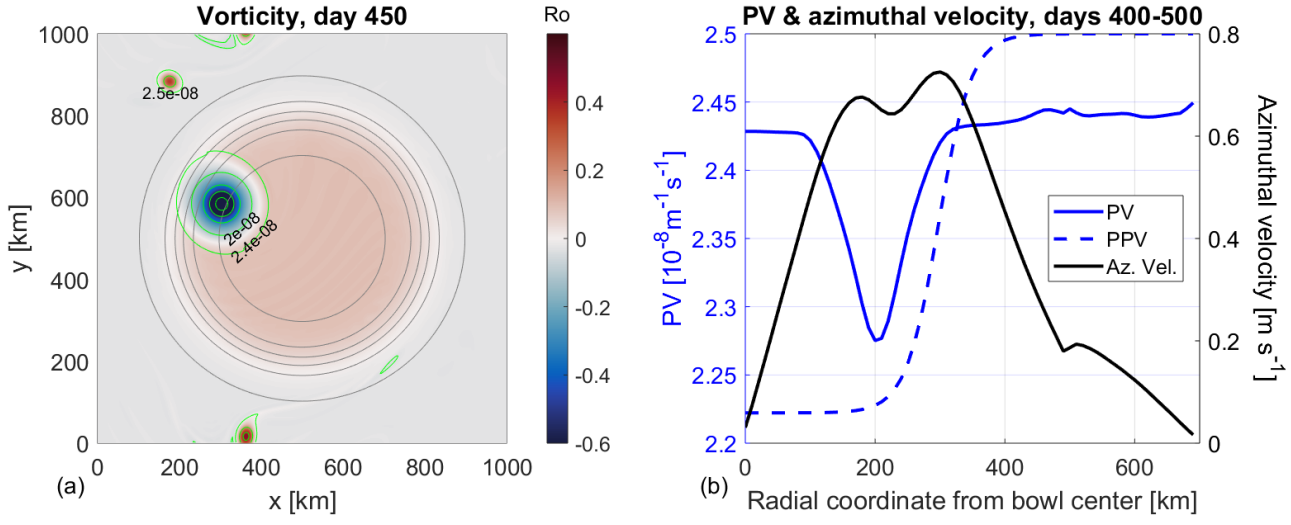

FIG. 6: Potential vorticity (PV) homogenization in an experiment ($B6E7$, table 1) with intermediate nonlinearity parameter value $\epsilon = 1.01$. (a) Vorticity (in f units) distribution at day 450 (in colors). PV contours are shown in green, with contours plotted at $[0.5,1,1.5,2,2.4,2.5]\times10^{-8}\mathrm{m}^{-1}\mathrm{s}^{-1}$. The $2.4\times10^{-8}\mathrm{m}^{-1}\mathrm{s}^{-1}$ contour approximately separates the low-PV trapped AC from its higher-PV surroundings. Topographic contours are shown in gray, at values of [4010,4100:100:4400,4490] m. (b) Radial profiles of potential vorticity (PV = $(f+\zeta)/H$, solid blue line), planetary PV (PPV = f/H, dashed blue line), and azimuthal velocity (black line) averaged over days 300–500. PV is homogenized on the slope region, thus eliminating the vortex cross-slope beta-drift. The anticyclone is advected counter-clockwise (at constant bowl radius) by the cyclonic slope current. Vortex self-advection in the presence of bathymetry (appendix A) also contributes to the cyclonic drift.

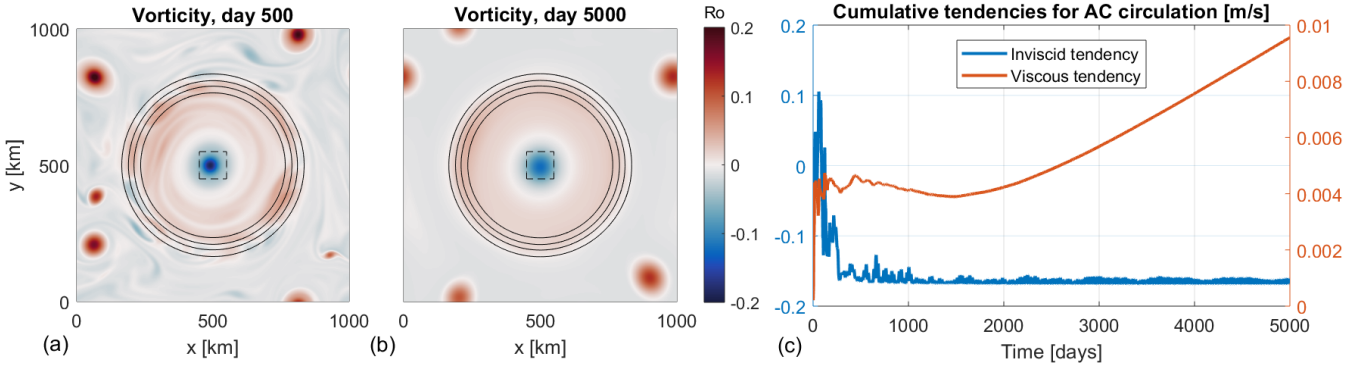

FIG. 7: Long-time evolution of bowl-trapped anticyclone. Panels (a) and (b) show the instantaneous vorticity (in f units) distribution at days 500 and 5000, respectively, for experiment $B1E3L$. Topographic contours (4100,4200,4300,4400 m depth) are shown in solid lines. The dashed square line in panels a–b shows the line along which circulation tendencies are calculated in panel c. Panel c: time-*cumulative* inviscid (blue) and viscous (red) circulation tendencies inside the bowl (just outside the anticyclone peak velocity radius, along the dashed lines of panels a–b). The cumulative tendencies are normalized by the perimeter of the dashed square such that they have dimensions of mean velocity, i.e., m/s.

In our simulations the latter occurs around the position of maximal topographic slope, $r = R_b$. The equations for $C_{AC} \equiv C(r_{AC})$ and for $C_{SC} \equiv C(r_{SC})$ then follow from (7a)-(7b):

$$\partial_t C_{AC} = -I(r_{AC}), \tag{8a}$$

$$\partial_t C_{SC} = -I(r_{SC}), \tag{8b}$$

$$\partial_t M_s \equiv \partial_t \int_0^{2\pi}\int_{r_{AC}}^{r_{SC}} \zeta\, dA = I(r_{AC}) - I(r_{SC}). \tag{8c}$$

Between the radii of maximal AC and slope current velocities ($r_{AC} < r < r_{SC}$) the late-time vorticity is positive (figures 3 and 7), principally due to the slope current. The trapped AC in our experiments typically has only a weak[8] "shield" of positive vorticity surrounding it (McWilliams 2006). The quantity M_s measures the slope current strength removing the AC integrated vorticity (by the Stokes theorem, equation 7a), and thus is a preferred slope current metric compared with C_{SC}. Therefore equation 8c shows that the slope current evolution ($\partial_t M_s$) has positive contributions from two flux integrals, i.e., at the slope region ($-I(r_{SC})$) and in the bowl interior ($I(r_{AC})$). Since C_{AC} decreases over time (as the anticyclone forms), we diagnose $I(r_{AC}) > 0$ for the $\epsilon \lesssim 1$ experiments of section 3b. Likewise, since C_{SC} increases over time (as the cyclonic slope flow forms), we diagnose $I(r_{SC}) < 0$. We conclude that the spin-up of the retrograde bowl anticyclone is necessarily associated with an eddy vorticity flux of equivalent magnitude at r_{AC} driving the slope current. That is in addition to spin-up due to contributions of eddy-fluxes at the slope region (r_{SC}).

In figure 8a we compare the time evolution of the circulations C_{AC} and C_{SC} in experiment $B1E5$ (compare with figure 4a). These are equivalent to the two cumulative eddy-flux tendencies forcing the slope current strength metric M_s. First, in panel (a) it is seen that both eddy fluxes have similar evolutionary time scales. Second, the exterior (r_{SC}) fluxes are larger in magnitude (see below). These qualitative observations occur across all the experiments (table 1). The role of eddy fluxes as a function of position ($I(r)$, equation 7b) is examined in panel b. This panel shows cumulative change in circulation over days 150-250 ($\approx \int_{t_1}^{t_2} I(r,t)dt$), selected because $|C_{AC}|$ gains most of its amplitude during this time, as a function of r. It is seen that the locations r_{AC} and r_{SC} are indeed associated with approximately the largest cumulative eddy fluxes. Over this period the eddy vorticity fluxes at r_{AC} and at r_{SC} have similar sized contributions to the slope current metric M_s.

Figure 8a shows that the magnitude of the late-time bowl AC circulation is around 1/3 of that of the slope current. Therefore, by the above analysis inner bowl fluxes ($I(r_{AC})$) supply approximately 1/4 of the cyclonic vorticity that accumulates on the inner bowl slope (M_s). The remainder is contributed by slope-region fluxes ($I(r_{SC})$). We suggest that the larger contribution from external fluxes ($I(r_{SC})$) relative to internal fluxes ($I(r_{AC})$) is largely a geometrical effect, due to larger area outside of the bowl. If this is the case then the slope current circulation should equal the anticyclone circulation, scaled by the appropriate area from which external fluxes are sourced: $C_{SC,\text{theory}} \approx -C_{AC} B^2/\pi r_{SC}^2$ (figure 8, dashed line). Here

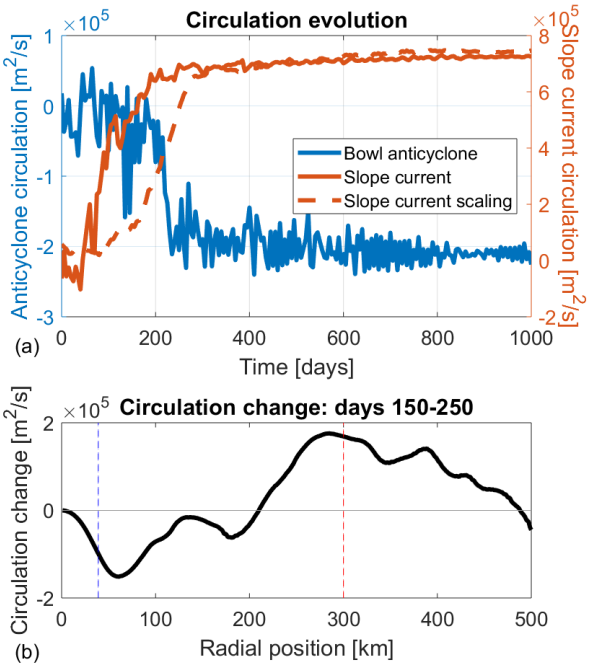

FIG. 8: Evolution of the circulation in experiment $B1E5$. (a) Circulation time series at bowl radii corresponding to the bowl anticyclone ($C_{AC} = C(r_{AC})$, in blue) and to the slope jet ($C_{SC} = C(r_{SC})$, the red solid line). In this experiment we diagnosed $r_{AC} = 39$ km. The reader is referred to equations (7a)–(8b) for the definitions of C_{AC} and C_{SC}. The dashed red line is a theoretical prediction for the slope current circulation based on the anticyclone circulation alone ($C_{SC,\text{theory}}$, see text). Compare with figure 4a. (b) Cumulative circulation change, due to eddy vorticity fluxes (dissipation is negligible), during the period of AC formation (from t_1=150 to t_2=250 days) as a function of radial position , *i.e.*, $C(r,t_2) - C(r,t_1) \approx -\int_{t_1}^{t_2} I(r,t)dt$. See equations 7a–7b. In panel b, the radii of the AC and slope current time series of panel a are marked with blue and red vertical lines, respectively.

$B = 1000$ km is the domain length. Indeed, in the figure C_{SC} and $C_{SC,\text{theory}}$ agree to within 3% at later times. In other experiments (table 1), the agreement is typically within ~20%.

4. Cross-slope motion and PV segregation

Our findings in §3 suggest that material transport is fundamental to the formation of the bowl central anticyclonic circulation. Indeed, the AC grows in our experiments through eddy mergers, and nonlinearity appears to be necessary (section 3a and appendix B). Furthermore, PV (a materially conserved quantity) is anomalously low

[8] In the reference experiment $B1E5$ for example, the AC shield has an integrated vorticity just 20% the magnitude of the integrated negative vorticity of the AC interior.

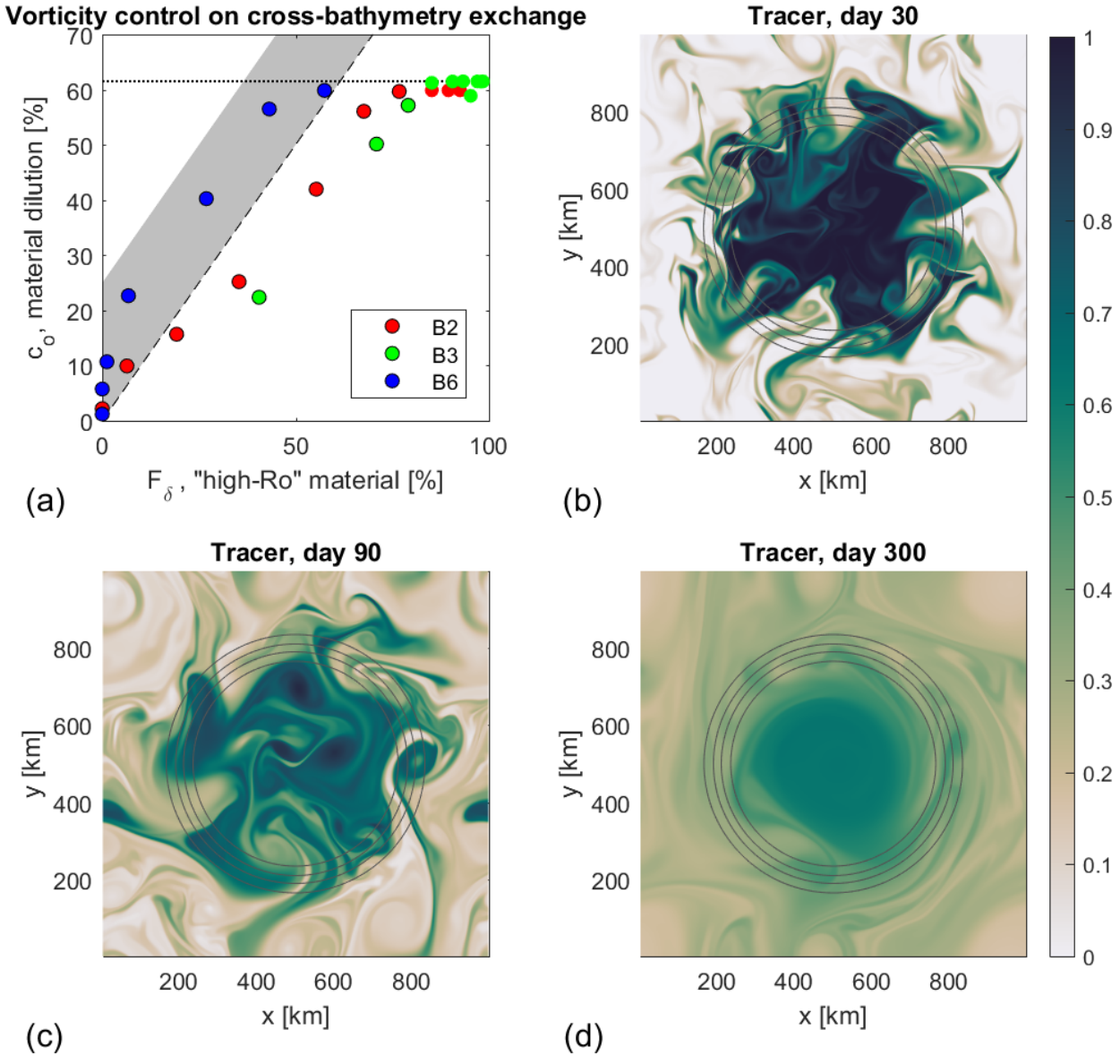

FIG. 9: Contribution of anticyclones originating outside the bowl to the bowl-trapped anticyclone. (a) Anticyclone material fraction originating from outside of bowl (c_o), versus F_δ: the percent of initial material with $\delta = H\zeta/fh \geq 1$, i.e., anomalously high Rossby (Ro) number. The fraction c_o is estimated from the late-time tracer concentration c averaged between $r = 0$ and $r = R_b/2$, since initially $c = 1$ (0) inside (outside) of the slope region, with a transition region on the slope. Experiments in which a trapped anticyclone forms are shown by a black edge to the marker. The horizontal (dotted) line shows the maximal dilution possible in case of homogeneous final state. Different experiment batches (table 1) are denoted by different colors (legend). The diagonal (solid) line shows a hypothetical $c_o = F_\delta$ relation. The amount of bowl anticyclone material in the final state originating from outside the bowl is quite close to the fraction of material with initial $\delta \geq 1$. Deviations above the unit line are likely partially due to material originating over the narrow slope region, where $0 < c < 1$ at $t = 0$. The maximal possible bias due to this effect is shown by the gray area. (b–d) Simulated tracer concentrations at three different times for experiment $B2E4$. Topographic contours (4100,4200,4300,4400 m depth) are shown in solid lines.

within the emergent AC (sections 3a-b). Here we address the following questions: Are all ACs that participate in central AC formation initiated within the bowl at $t = 0$, or do some enter from outside of the bowl? If the latter, what are the mechanisms via which they transition from outside to inside the bowl?

a. Cross-bowl material transport

First, we examine the amount of cross-bowl material transport which occurs in the process of AC evolution using passive tracer deployments. The tracer is initialized (section 2b) with a radial tanh profile, with values close to 1 (0) inside (outside) of the bowl. Therefore a final average value $c = c_b < 1$ within the bowl center (diagnosed at $r \leq R_b/2$), implies that the fraction of material in the same area which originated outside the bowl is $c_o = (1 - c_b)$.

An anticyclone can maintain its coherence while crossing the slope into the bowl only if its vorticity (ζ) is high enough to avoid destruction by vortex stretching. Therefore crossing requires $\delta = H_0|\zeta|/fH_B \geq 1$. We test this in figure 9, which shows that the amount of bowl anticyclone material in the final state originating from outside the bowl is approximately proportional to F_δ, the fraction of material with $\delta \geq 1$ at $t = 0$. For small enough F_δ virtually no material is exchanged across the slope, and the AC forms only from material originally present within the bowl. At higher F_δ values, a substantial fraction of the late-time material in the AC originates outside the bowl.

The interpretation of the late-time tracer concentration is complicated by the initial $O(50\text{km})$ wide tracer transition area on the bowl slope, where $0 \leq c \leq 1$. Due to this transition region, in a hypothetical end state in which no material is exchanged across $r = R_b + 2W_b$ (at the 98th depth percentile) and all material in $r < R_b + 2W_b$ is well mixed, the bowl tracer concentration would be $c \approx 0.75$. Hence we estimate the maximal possible bias from the tracer transition region via an added dilution of 25%, shown by the gray area in figure 9. Another complication is that in a finite domain only a finite maximal dilution can occur; this is also marked in figure 9 by the dotted line.

In cases with small F_δ, the anticyclonic vortex growth still occurs by via repeated vortex mergers, but only emerges from AC eddies that are already in the bowl at $t = 0$. We observe (not shown) that anomalously high-PV material (*i.e.* cyclones) initially inside the bowl ultimately transit to the slope region, either as part of the cyclonic slope current, or as a coherent cyclonic eddy embedded within the slope current. Stability of cyclonic eddies within the inner part of the slope current (for small F_δ) is generally consistent with the results of Marcus (1990), as we diagnose $\sigma > 0$ in the inner slope region in these cases. The sign is opposite to that reported for experiment B6E7 (section 3b(ii)). To see why, note that cyclonic slope current velocity peaks close to the slope center. Hence strain $\sigma = r\partial_r(v/r)$ is (negative) positive in the inner slope region if the velocity peak is locally (less) more sharp than a linear profile. Weak ϵ (and F_δ) results in weak PV homogenization, and hence in sharp slope currents, and vice versa, consistent with the diagnosed signs in each case.

In cases where F_δ is large enough, cross-slope motion may be induced by at least two processes in the present experiments: 1. Monopole vortex (topographic) beta drift (Carnevale et al. 1991); 2. Dipole propagation. Rather than attempting to determine the fraction of monopole and dipole (or multipole) interactions contributing to the AC formation in our turbulent experiments, we concentrate on a more tractable task. We present results from topographic bowl experiments initialized with a single monopole or dipole (section 2c), and compare the cross-topography propagation speed of each. For brevity, in each case a single illustrative experiment is presented, along with formulae for propagation speeds in the general case.

b. Monopole topographic beta-drift

McWilliams and Flierl (1979) found that barotropic QG vortices on a beta plane (with constant β) drift meridionally (equivalently, cross-slope on a topographic β plane) with speed $\sim \beta r_0^2$, where r_0 is the vortex radius (or, more generally, the pressure e-folding scale). It is not clear to what extent these results should hold for a finite-width and curved bottom slope. In this case we define a cross-slope vortex (monopole) propagation speed ($v_{m,1}$) predicted from the local topographic beta value, $\beta(\mathbf{x}) = -(f/H)|\nabla H(\mathbf{x})|$:

$$v_{m,1}(\mathbf{x},l) = \beta(\mathbf{x}) r_0^2. \tag{9}$$

However, vortex beta drift is driven by a secondary vorticity field which is set up by the vortex as it advects material a finite distance across f/H contours. Therefore, it may be that the relevant β value for vortex drift is to be evaluated in a region around the vortex rather than at its center. Thus we also test a second hypothetical speed,

$$v_{m,2}(\mathbf{x},l) = <\beta(\mathbf{x})> r_0^2, \tag{10}$$

where <> marks an average over the area defined by $r_0 \leq r_v \leq 2r_0$, with r_v = distance from vortex center.

Expressions $v_{m,1}$ and $v_{m,2}$ are compared with the diagnosed vortex down-slope propagation speed, $v_{m,e}$ for a vortex of radius $r_0 = 45$ km initialized outside the bowl in figure 10a. Indeed, the approximate non-local generalization of the beta drift term, $v_{m,2}$, compares quite well with the diagnosed speed up until the vortex arrives at the middle of the slope. In comparison, $v_{m,1}$ is considerably lower outside the bowl. After the vortex reaches the middle of the slope region, both of the above formulae fail to reproduce its subsequent propagation speed. The vortex acquires a weak dipole component as it propagates across the

slope (McWilliams and Flierl 1979), which survives into the flat interior region. The companion is largely responsible for the deviation between the theoretical predictions and the diagnosed propagation speed, as are the presence of a slope current and topographic Rossby waves induced by the passage of the vortex.

c. Dipole propagation

Dipoles propagate perpendicular to their eddy-separation axis. Topography causes an asymmetry in their dynamics such that propagation in the down-slope direction often results in the anticyclone shedding into the depression while the cyclone is repelled outside (Carnevale et al. 1988).

The trajectory of the anticyclone from a representative dipole experiment (see section 2c) is shown in figure 10b. Here the initial mean vorticity in each vortex is 0.25 f, and the dipole orientation was chosen such that the dipole propagates directly towards the bowl. The dipole propagates towards the bowl until the cyclone is shed upon arrival at the bowl slope (Carnevale et al. 1988) between days 15-20, after which the anticyclone continues downslope and the cyclone is eventually ejected upslope. It is seen that away from the bowl rim, the dipole travels considerably faster than the monopole in panel a. For example at 1.5 bowl radii away ($r = 1.5R_b$) from its center (with present slope half-width parameter $W_b \approx R_b/6$) the dipole is an order of magnitude faster than the monopole. The dipole is initialized at a greater distance than the anticyclone to illustrate this difference further.

The dipole speed can be predicted based on a theoretical model of point vortices (McWilliams 2006; Kloosterziel et al. 1993). The point model predicts a dipole speed $v_d = \frac{C}{2\pi d}$, where C is the strength (peak circulation) of each vortex, and d the pair separation distance. The value of v_d is estimated based on diagnosis of these parameters from the dipole experiment. Its value generally agrees well in order of magnitude with the diagnosed anticyclone downslope drift speed before the cyclone is shed. The dipole begins somewhat slower than v_d and overshoots its value slightly. This may be explained by that the initialized state is comprised of two superposed monopole vorticity fields, and hence some initial adjustment occurs. The adjustment process results in a smaller d, which explains the faster velocity at later times.

In summary, in this subsection it is shown that a bowl trapped anticyclone can form either locally from material initially present within the bowl, or also by sourcing material from outside the bowl. The percentage of externally sourced material depends largely on F_δ, the fraction of the initial anticyclonic vorticity that exceeds the topographically-imposed vorticity change. Anticyclones that enter the bowl can do so via either monopolar or dipolar propagation. It is shown that dipole cross-slope propagation can be considerably faster than monopole topographic beta drift former under certain conditions. For the monopole case, due to the non-uniform bottom slope, an approximate generalization the constant-slope formula is suggested, and reasonably matches the diagnosed speed.

5. Two-layer experiments

In this section we report the results of our 2-layer experiments — the minimal configuration that permits baroclinity. We examine whether a bowl AC forms in baroclinic conditions, and diagnose its vertical structure as a function of system parameters. The very long lived ACs observed in the ocean above depressions (section 1) are surface intensified (note their velocity maximum commonly occurs at depths of $\sim 500\ m$), but a non-negligible barotropic component is observed as well (Mann 1967; Willis and Fu 2008; Köhl 2007; Fer et al. 2018; Bosse et al. 2019; Le Corre et al. 2019). In our idealized barotropic experiments AC formation depends strongly on topographic effects, and it is unclear whether this should favor a surface-intensified trapped AC structure.

Several batches of experiments were conducted. Stratification parameters were varied between batches, and the initial vertical structure was varied within each batch. For brevity we report mainly on a reference batch (hereafter B_{BC1}, BC standing for "baroclinic") of experiments with $\lambda_0 = 90$ km, upper layer rest thickness $H_1 = 1000$ m, and topographic parameters $R_b = 300$, $W_b = 50$, $H = 2$, and $H_b = 0.5$ km. The reduced gravity is set to $g' = 10^{-2}\ m/s^2$, resulting in a baroclinic Rossby deformation radius of $L_d = \sqrt{g' H_{eq}}/f = 22$ km (McWilliams 2006). Here the equivalent depth $H_{eq} = H_1 H_2/H$ is used, with $H_2 = H - H_1$. These parameters are loosely motivated by the Mann Eddy basin (see also section 2b). The Rossby deformation radius in the top (bottom) layer is $L_{d,1} = \sqrt{g' H_1}/f = 27$ ($L_{d,2} = \sqrt{g' H_2}/f = 38$) km.

The initial kinetic energy densities of the top and bottom layers (E_1 and E_2 [m^2/s^2] , respectively) were varied between the B_{BC1} batch experiments, taking the following relative values: $(E_1,E_2)/E_0$ = (0,1), (0.25,1), (0.5,1), (0.75,1), (1,1), (1,0.75), (1,0.5), (1,0.25), (1,0). These experiments were repeated with two different kinetic energy densities in the dominant layer: $E_0 = 0.01$ or $E_0 = 0.1$ [m^2/s^2]. In each experiment, the random initial phases θ_k were generated independently in each layer.

We find that a bowl-trapped AC forms in all B_{BC1} experiments. A specific example of the evolution is shown in figure 11, from the B_{BC1} experiment with $E_2 = 0$ and $E_1 = 0.1$ [m^2/s^2]. By day 30 the circulation has largely barotropized as is generally expected for circulation features larger than the deformation radius (Salmon 1998). By day 250 a single coherent AC is formed near the bowl

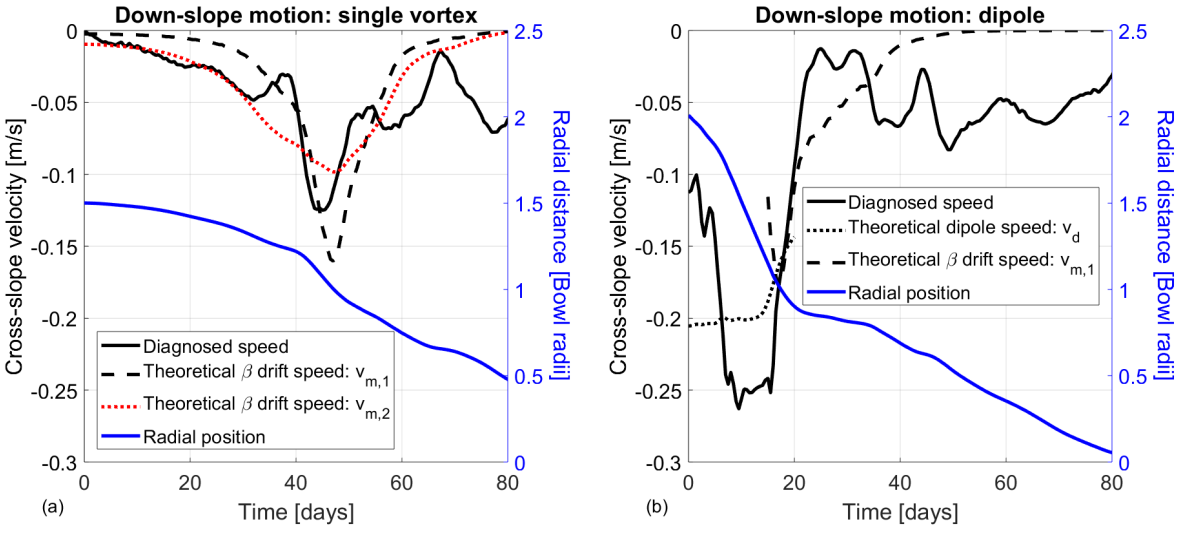

FIG. 10: Coherent vortex propagation experiments. (a) A monopole vortex experiment. Diagnosed vortex down-slope velocity (solid black line) is compared with two different theoretical vortex down-slope beta-drift velocity estimates (equations 9 and 10, shown by dashed and dotted lines, respectively). The radial position from bowl center is shown in blue (right-side axis). (b) As in panel (a), but for a dipole experiment. The theoretical dipole speed is shown by the dotted line. The initial conditions for the dipole are: mean vorticity within each dipole vortex of magnitude 0.25 f; vortex radii $d = 45$ km; vortex separation = $2.6d$.

center. It is top intensified but has a substantial barotropic component. Topographic Rossby waves (TRW), straining of eddies on the slope, and the emergent slope current all appear to be bottom-intensified.

More generally, we find that the trapped AC tends to be top (bottom) intensified for top (bottom) intensified (random) initial conditions. Vertical structure results are presented in figure 12, in terms of a surface intensification metric: $S \equiv \log(v_1/v_2)$, where v_i is a velocity magnitude in layer i. For the initial S metric, S_0, v_i is defined as the initial time spatial-RMS velocity value. For the final S metric, S_f, v_i is defined as an average over the last 100 days of azimuthally-averaged azimuthal velocity at the radius of peak eddy velocity (for the AC), or at mid-slope (for the slope current). In contrast to the AC, the slope current is consistently bottom-intensified, with a similar value of final S value in all B_{BC1} experiments. Following these diagnosed trends, we suggest simple scaling rules for top intensification of the AC and slope current.

Scaling for the slope current vertical structure. We assume that the slope current is induced by TRW rectification (Brink 1986; Beckmann and Haidvogel 1997). Hence, the slope current vertical structure may be expected to be similar to that of the waves. The upper layer QG PV equation for TRW is[9]

$$\partial_t \left(\nabla^2 \psi_1 - L_{d,1}^{-2} \psi_1 + L_{d,1}^{-2} \psi_2 \right) = 0. \qquad (11)$$

[9]Here we linearize around the initial state of approximate zero mean flow along isobaths.

Here upper and lower layer quantities are denoted by $i = 1$ and $i = 2$ subscripts, respectively. For any wave mode (with nonzero frequency) the expression within the parentheses need be identically zero. Therefore,

$$\psi_2 = (1 - L_{d,1}^2 \nabla^2) \psi_1. \qquad (12)$$

Over an isolated topographic feature TRW generally vary with scales similar to the topographic variation length scale, which we take as the slope half-width W_b (section 2b). Hence $\nabla^2 \sim -W_b^{-2}$, resulting in

$$\psi_1 \sim \frac{1}{1 + (L_{d,1}/W_b)^2} \psi_2. \qquad (13)$$

The relation is similar to a Taylor Cap height over seamounts with continuous stratification (Hogg 1973). Statistical turbulence theories (Salmon et al. 1976) predict functionally-similar, although not identical, relations.

Scaling for the anticyclone final vertical structure is suggested for the cases in which one layer is initially at rest ($S_0 = \pm\infty$). Suppose conditions are initially surface intensified, i.e., $\psi_2(t = 0) = 0$ and $S_0 = \infty$. Then initially the lower layer evolution is approximately described by the linearized QG equation,

$$\partial_t \left(\nabla^2 \psi_2 - L_{d,2}^{-2} \psi_2 \right) = -\partial_t L_{d,2}^{-2} \psi_1 - J(\psi_2, h). \qquad (14)$$

With random initial conditions we may assume $\psi_1(t = 0) \approx 0$ at the bowl center. We also assume that the topographic

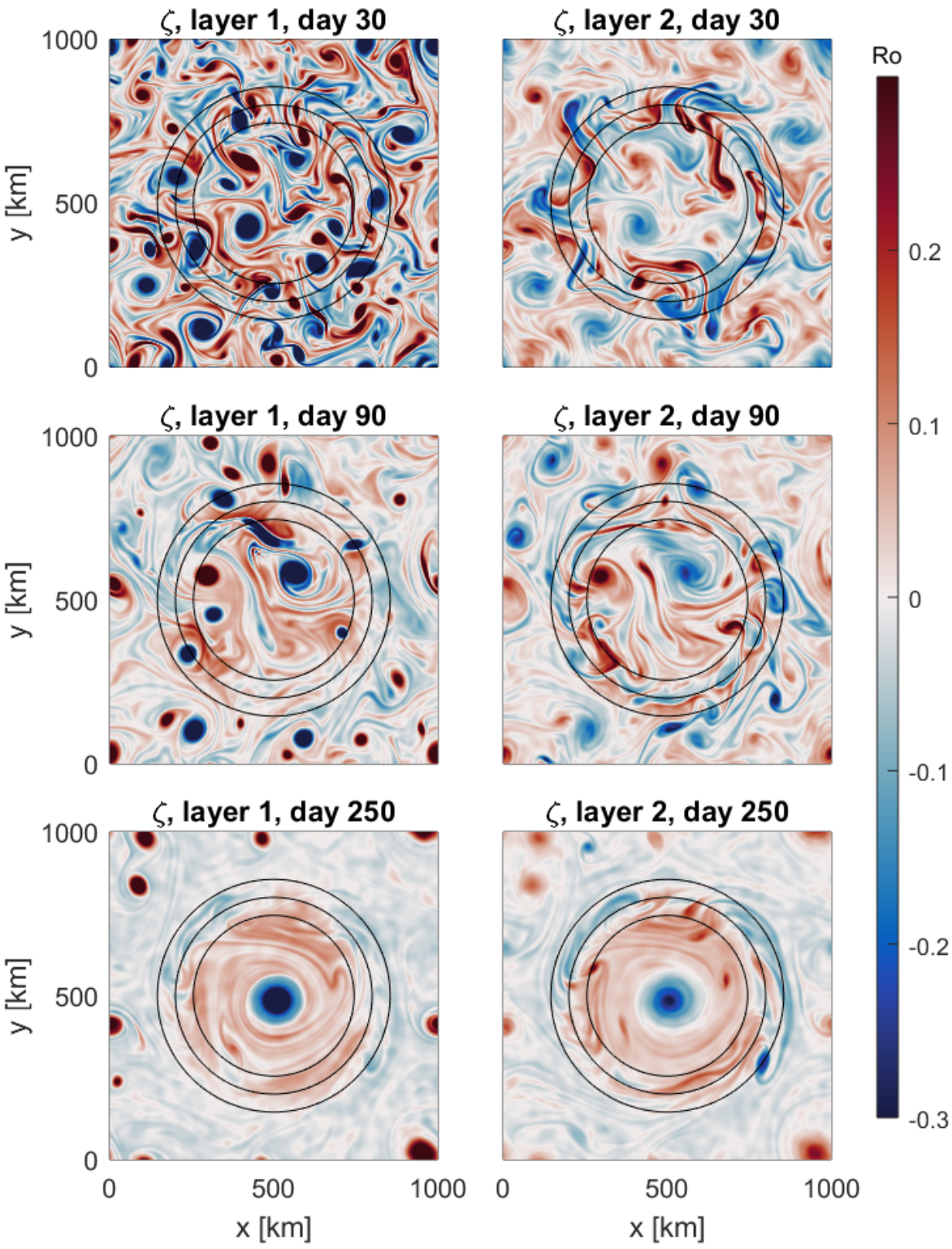

FIG. 11: Vorticity (in f units) snapshots in a 2-layer experiment, with initial (at day 0) zero kinetic energy at the lower layer. Layer number (layer 1 is the top layer) and number of days since initialization are indicated in each panel. Black contours show the (2050,2250,2450) [m] isobaths.

term will be initially negligible since $\psi_2(t=0)=0$ and since the topography is weak at bowl center. Therefore, in this case the AC amplitude in the lower layer follows from

$$\left(\nabla^2\psi_2 - L_{d,2}^{-2}\psi_2\right) = -L_{d,2}^{-2}\psi_1. \quad (15)$$

Assuming that horizontal structure is dictated by the energy-dominant layer, a scale estimate results by setting $\nabla^2 \sim -r_1^{-2}$, where r_i is the AC core radius in layer i[10]. The eddy core radii r_i are diagnosed in each case (section 2d), and are typically 35–60 km in these simulations. Therefore

$$\psi_1 = \left[1 + (L_{d,2}/r_1)^2\right]\psi_2. \quad (16)$$

For a case with $S_0 = -\infty$, the late-time scaling resulting from similar reasoning is

$$\psi_1 = \frac{1}{1 + (L_{d,1}/r_2)^2}\psi_2. \quad (17)$$

The top intensification scaling for the slope current and for the AC are examined against the B_{BC1} numerical experiments results in figure 12. The scaling laws predict the right sign of S_f, i.e., top or bottom intensification. The slope-current prediction (equation 13) is indeed very close to the numerical final state S_f, for all examined S_0 values. The AC S scaling relations, (16) and (17), are of the right S_f sign and order of magnitude (within 7-40%) in all applicable cases (i.e., $S_0 = \pm\infty$).

The scalings (13)-(17) all share a dependency of the form L_i/l, where l is the relevant circulation feature length scale. Hence we conducted additional experiment batches varying the Rossby radii $L_{d,i}$ (e.g., by changing stratification). Cases with much higher Rossby radii of order $100-150$ km were attempted. The AC core radii r_i were < 90 km in all cases. We find that trapped anticyclones still form in cases with $S_0 < \infty$, and in some cases with $S_0 = \infty$ [11]. The trend predicted by the scaling relations is correct in these cases, i.e., top or bottom intensification is more acute relative to B_{BC1}, by as much as on order of magnitude. The scaling relations also predict the right S order of magnitude in each applicable case. The scatter in S is however relatively larger than in B_{BC1}, and we do not attempt a further systematic exploration.

To test the longevity of the trapped AC, similarly to the 1 layer experiment in section 3c, the duration of the B_{BC1} experiments with $S_0 = \pm\infty$, 0 and with $E_0 = 0.1$ [m^2/s^2] were extended - from 500 to 3000 days. The main qualitative result (not shown) is that the AC and slope current both survive largely unchanged throughout the experiment. The results are quite similar to the 1-layer case[12]. Some diffusion of the trapped AC occurs: the trapped AC peak vorticity in each layer decreases by 10–30% between days 500 to 3000 while its radius expands. In each layer again, the integrated circulation of the contiguous patch of negative-vorticity around the AC center does not change by more than 1%, while that of the core grows by several tens of percent. Implications are discussed in the next section.

6. Discussion - complex topography and topographic turbulence theories

All numerical experiments discussed above involved an isolated and functionally simple topographic feature. Real ocean topography is characterized by multiple scales and roughness. Hence, experiments with non-isolated topography were conducted as well. Complex topographic shapes were created using a similar random formula to (2) (e.g., figure 13). Cyclonic (anticyclonic) circulations emerge on the slopes of the topographic depressions (bumps), i.e., slope currents, consistent with previous results (e.g., Bretherton and Haidvogel 1976). However, embedded within the interiors of these large scale circulations, we find that coherent ACs (cyclones) with anomalously low (high) PV appear at the center of some or all topographic depressions (bumps) in each experiment. The trapped coherent eddies emerge as long as λ_0 is small enough (e.g., a factor of ≈ 5 was sufficient) relative to the analogous typical topographic wavelength (λ_t). This condition, as well as numerical resolution, may explain the lack of previous reports on these vortices in similar numerical simulations. Results from one of our random topography experiments are shown in figure 13. We note that in some random topography experiments (including in figure 13) not all topographic (depressions) bumps contain a clear interior (anti)cyclonic vortex. That is to be expected since the trapped vortices have anomalous PV values (sections 3a-b). The limited reservoir of anomalously-valued PV material did not produce a sufficient number of vortices to populate all topographic features, but we did not explore the dynamics or statistics of this partitioning in detail.

We also conducted experiments with isolated topographic features lacking a significant central flat region of size larger than an eddy size. That is of interest relative to seamount circulation (section 1). An example of an "inverted seamount", a Gaussian topography with 50 km standard deviation, is shown in figure 2. Results are not shown here graphically in the interest of space. In this case the prograde slope current manifests as a cyclonic eddy (Taylor Cap), as predicted by seamount circulation theory (section 1). Additionally, we find that trapped (ACs) cyclones can emerge over the slope regions of such (inverted) seamount shapes, and propagate with the slope current at a constant radius. This occurs when partial homogenization

[10] This scaling is exact in case of a vortex core in solid body rotation, e.g., a Rankine vortex.

[11] Time-scales to (partial) cross-layer coupling grow with L_i/l magnitude, and with S_0 magnitude, which makes simulation more demanding and complicates analysis of the results.

[12] The comparison is only qualitatively informative since the parameters H_0, E_0, and λ_0 differ between these experiments.

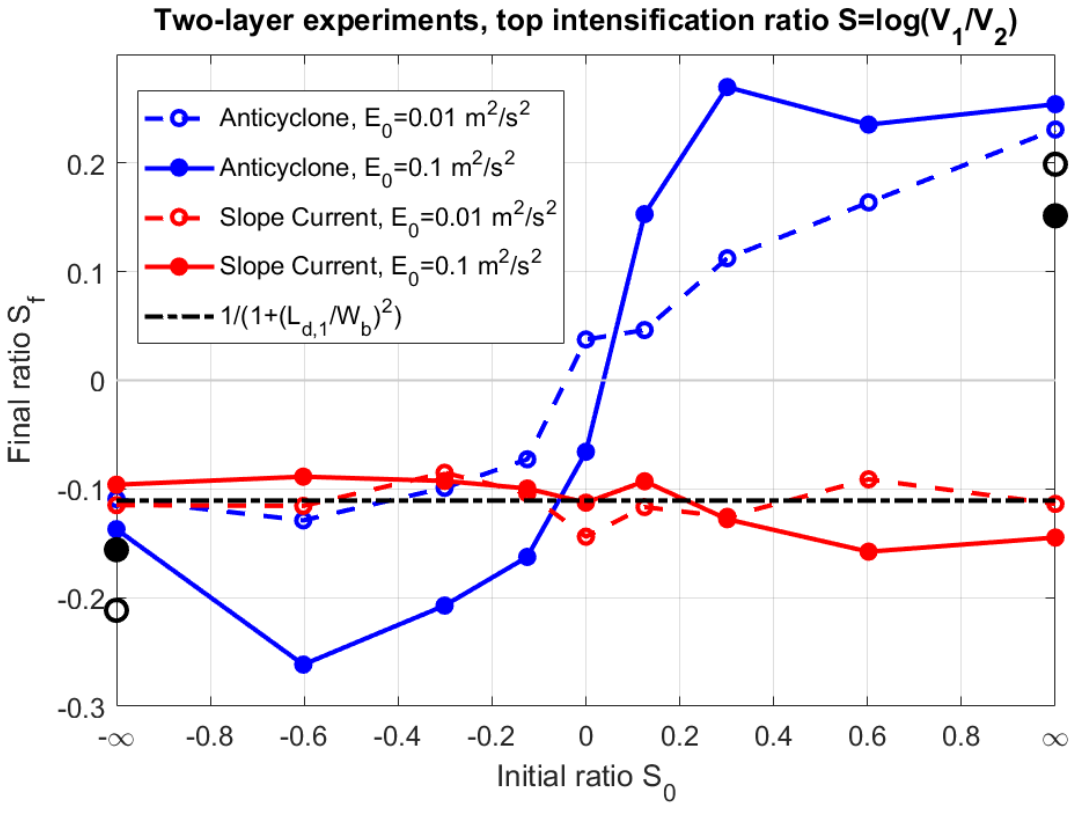

FIG. 12: Vertical structure of the bowl-trapped anticyclone and of the slope current in two-layer experiments. A surface-intensification metric, $S = \log(v_1/v_2)$, is shown for the initial conditions (S_0, x-axis) vs. the final state (S_f, y axis). Here v_1 (v_2) is the velocity magnitude in the top (bottom) layer. Hence, e.g., $S = -\infty, 0, \infty$ for cases with $v_1 = 0$, $v_1 = v_2$, and $v_2 = 0$, respectively. Initial velocity magnitudes are the prescribed RMS random velocities. Final velocity magnitudes are defined as azimuthally-averaged azimuthal velocity, either in the core of the slope current or at the radius of the anticyclone's maximum azimuthal velocity. The vertical structure of topographic Rossby waves (dashed-dotted black line) closely predicts the slope current structure regardless of the initial conditions. Scaling estimates for the final anticyclone vertical structure in the limits $S_0 = -\infty$ and $S_0 = \infty$ (equations 16 and 17, respectively) are shown by isolated black circle symbols. Dashed lines and empty circles (solid lines and filled circles) denote cases with initial kinetic energy in the intensified layer of value $E_0 = 0.01$ (0.1) [m^2/s^2].

of the PV field is achieved, i.e., the cause is similar to the $0.5 \lesssim \epsilon \lesssim 1$ regime of section 3b, and may explain similar observations in the experiments of Carnevale et al. (1991).

As summarized in section 1, topographic turbulence theories broadly predict that (anti)cyclonic circulation should form over (bumps) depressions. These predictions have been verified in previous idealized numerical simulations (Bretherton and Haidvogel 1976; Salmon et al. 1976; Merryfield 1998; Majda and Wang 2006; Venaille 2012) and in the present study. However, these theories do not predict a circulation of opposite polarity in the interior of closed topographic contours, *i.e.* they do not predict the formation of the bowl-trapped AC in our experiments.

A fundamental feature of these topographic turbulence theories is the prediction of a single-valued (i.e., monotonic) streamfunction (ψ) to PV (q) relation (Bouchet and Venaille 2012). To the contrary, we find the relation is multiple-valued in our simulations (e.g., figure 4b). It is clear that the multiple-valued $\psi - q$ relation is due to the cross-over from the bowl AC to the slope jet. Hence the theories cited above cannot predict these two features together. Earlier numerical random topography simulations (Bretherton and Haidvogel 1976) did exhibit differing, quasi-linear, $\psi - q$ relations over different subdomains. However, we find a qualitatively different, multi-valued $\psi - q$ relation within a single isolated and smooth topographic feature. A deviation from single-valued $\psi - q$ relations in idealized simulations was also previously reported by Vallis and Maltrud (1993), associated with alternating jets parallel to steep topography.

A possible explanation for the disagreement of our results with topographic turbulence theories is that the AC (unlike the slope current) is a transient feature, and hence should not be predicted by equilibrium theories. However as shown in sections 3c and 5, the trapped AC circulation does not decay by a measurable amount over a time scale of at least ~ 10 years. In barotropic numerical simulations of a closed basin with a "continental slope" close to the basin edges and a flat bottom in the center, the spin up of a center anticyclone was previously reported (Cummins and Holloway 1994; Shchepetkin 1995). In the case of Cummins and Holloway (1994), the center anticyclone decayed over a time scale equivalent to ~ 100 years. Cummins and Holloway (1994) argued that the decay occurred inviscidly. We note, however, that the AC evolution and the slope-current evolution are not completely independent, as the results of section 3d show. Finally, it is possible that this local coupling is not captured in the discussed topographic turbulence theories since they impose conservation laws only in an integrated sense, or with a mean-field approximation (Bouchet and Venaille 2012; Venaille 2012).

7. Summary and conclusions

In several North-Atlantic basins, long-lived and semi-stationary mesoscale anticyclonic vortices (ACs) have been observed repeatedly. These basins are characterized by bowl-like topography, i.e., slopes surrounding a much less steep central area. The ACs reoccur over periods of years to decades, and have a significant signature on mean regional properties (e.g., SSH, figure 1). Previous work suggested different dynamical mechanisms for AC formation and persistence in each of these cases.

Motivated by these observations, we conduct idealized numerical experiments of flow evolution over bowl-like topography to determine if and how trapped ACs evolve in a minimal complexity model. Primitive equation simulations with one or two isopycnal layers are conducted. Although many processes are neglected, the lighter computational burden facilitates multiple experiments, sweeping wide parameter ranges.

We find that a bowl-trapped AC does emerge spontaneously from random initial conditions under a wide range of circumstances. Typically this occurs through repeated mergers of ACs within the bowl interior, and the resulting trapped AC is characterized by anomalously low PV. Another general result, consistent with previous theory and simulations (the "Neptune" effect, section 1), is the emergence of a prograde slope current, corresponding to cyclonic circulation around a bowl.

To determine the robustness and parameter dependence of these phenomena, we conduct a large array of single-layer experiments. The initial kinetic energy and dominant initial circulation wavelength, as well as topographic shape parameters, are varied. A nonlinearity parameter (ϵ) is identified as largely determining the formation of a trapped AC in these experiments. This parameter is the ratio of vorticity scale to topographic vorticity stretching, and describes the relative effects of eddy-eddy interactions to topographic effects. The AC typically forms for $\epsilon \lesssim 1$, although it does not form for $\epsilon = 0$ (i.e., with advection terms neglected, as shown in appendix B). In the first regime, $\epsilon \lesssim 0.5$, the AC is confined relatively close to the bowl center. In the second regime, $0.5 \lesssim \epsilon \lesssim 1$, trapped ACs typically still occur, but may revolve around bowl-center at different distances $r \leq R_b$, depending on initial conditions. In the third regime, $\epsilon \gtrsim 1$, eddy-eddy interactions dominate, and vortices freely cross topographic contours.

To explain the varying radial positions of the bowl-trapped ACs, we introduced a second non-dimensional parameter, PVI, a metric of PV inhomogeneity (excluding the trapped AC PV signature). At small ϵ the radial PV gradient is dominated by the topography, and PVI ≈ 1. However, PVI generally decreases with increasing ϵ values, and in most cases satisfies PVI $\ll 1$ for $\epsilon \gtrsim 0.5$. The outcome is consistent with PV stirring and mixing by incoherent eddies, viewing the Lagrangian conservation of PV as approximately analogous to a passive tracer. A similar outcome was also predicted by Rhines and Young (1982) within closed mean ocean gyre streamlines, at depths such that non-conservative process are negligible, under the assumption that eddy fluxes cause a mean down-gradient PV diffusion. The erosion of background PV gradient in the bowl eliminates the topographic beta drift, which otherwise tends to push ACs toward the center of the bowl. Hence, for $0.5 \lesssim \epsilon \lesssim 1$, the AC can occupy any radial position within the region of homogenized PV, and be passively advected cyclonically by the slope current. We show that a relatively smaller contribution to the cyclonic drift of the AC occurs through a nonlinear eddy-topography SWE effect, which is not eliminated despite the homogenization of background PV.

While it is clear that AC mergers contribute to the trapped AC formation, it is not *a priori* clear whether these ACs should originate from inside or outside of the bowl. We show that the origins of the ACs that contribute to the bowl-trapped AC is set by a parameter F_δ (section 4), which quantifies the fraction of the initial anticyclones that are outside of the bowl and are sufficiently strong to cross the topographic PV gradient. We show through tracer analysis that for weak vortices, *i.e.* small F_δ, there is negligible exchange of material across the topography. The relative exchange and amount of final "dilution" of the inner bowl material, grows approximately linearly with F_δ.

Motivated by the role of anticyclones migrating into the bowl in forming the trapped AC, we isolated and examined two different mechanisms of cross-bowl transport: eddy (topographic) beta drift (Carnevale et al. 1991), and dipole

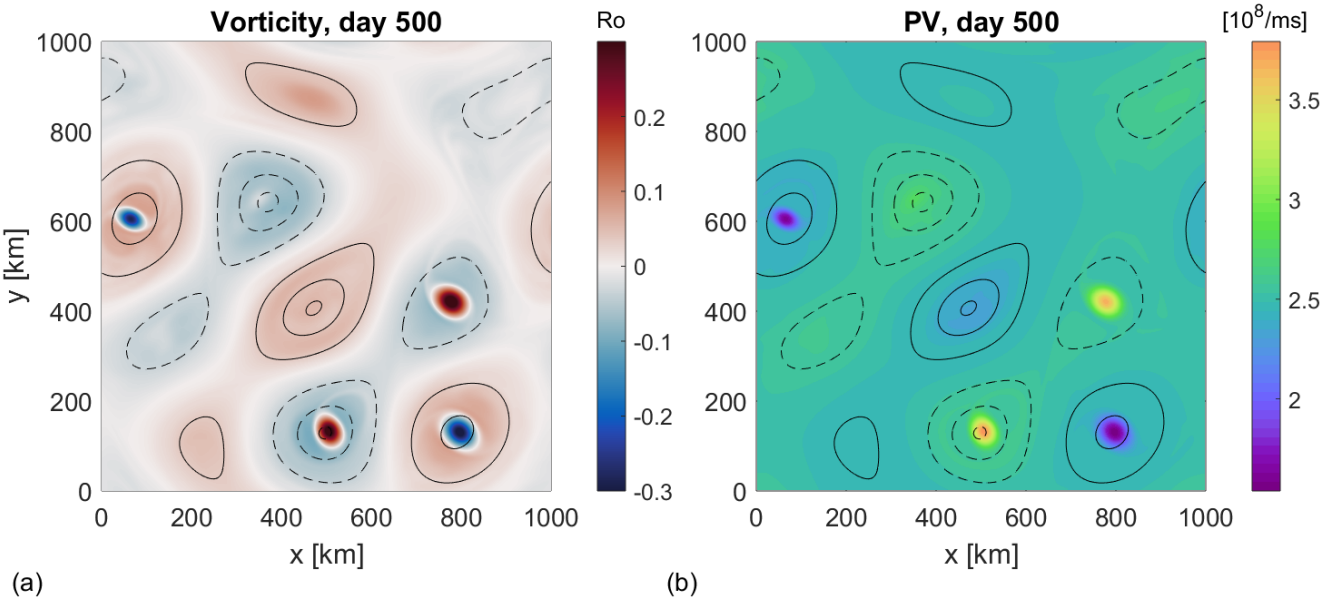

FIG. 13: Coherent vortices emerging within topographic anomalies in an experiment with complex topography. (a) Vorticity (in f units) and (b) potential vorticity (PV) after 500 days of free evolution. Dashed (solid) lines are elevated topographical areas (depressions) of height 200, 400, and 490 m above (below) a mean 4 km depth. Vorticity and PV are clearly influenced by the topography. Where relatively strong bottom slopes occur, the vorticity is positive at depressions and vice-versa. This is associated with development of slope currents, and is consistent with topographic turbulence theories (section 1). However, anticyclones (cyclones) tend to develop within centers of depressions (bumps), and are associated with anomalously negative (positive) PV. These central vortices are not predicted by topographic turbulence theories. Experiment parameters: $\lambda_0 = 45$, $\lambda_t = 400$ km, $E = 0.02$ [m^2/s^2], $\epsilon \approx 0.3$.

interactions (Carnevale et al. 1988; Kloosterziel et al. 1993). The former was previously suggested to be important in the case of the Lofoten AC (Köhl 2007). Using experiments with initial conditions of a single (monopole) AC, or of a close pair of opposite-signed eddies (dipole), we show that both mechanisms can allow anticyclones to enter the bowl. However, and dipole propagation is typically more efficient for reasonable parameter values, especially at larger distances from the bowl slope. We proposed an approximate generalization of previous theoretical monopole beta-drift to account for the variable topographic slope.

Two-layer experiments support the one-layer results on AC formation. We focus on the characterization of vertical structure of the emergent trapped AC, as well as of the slope current. We find that the emergent slope current is bottom intensified in all cases, to a degree determined by stratification conditions, similar to a Taylor Cap (Hogg 1973). In contrast, the emergent trapped-AC is bottom-intensified (surface-intensified) if domain-mean initial conditions are bottom-intensified (surface-intensified). The vertical structures of the observed ocean ACs (see section 1) are surface-intensified, with maximal velocities within the upper 1 km of the water column, and velocities decaying toward smaller but finite values near the sea floor. Thus an interpretation of our two-layer experimental findings is that the general tendency for ocean mesoscale eddies to be surface-intensified leads to surface-intensified trapped ACs such as the Mann and Lofoten eddies.

We find that, in the single layer experiments, the spin-up times of the bowl AC and the slope current are similar. Therefore, we examine the relation between vorticity and circulation evolution equations of both the AC and the slope current (section 3d). This relation shows that the vorticity fluxes driving the formation of the bowl AC also contribute to the spin-up of the slope current. Furthermore, although the slope current is accelerated by a second source of vorticity fluxes as well (from outside the bowl), the final bowl AC strength is a good predictor of the slope current strength. These relations suggest that the vorticity fluxes inside and outside of the bowl are both mediated by similar mechanisms.

In section 6 we contrasted our results with topographic turbulence theories. These theories predict the emergence of a prograde slope current, but not a bowl-trapped AC. We find that depression-trapped ACs also occur in simulations with complex topographies, similar to experiments previously used to test topographic turbulence theories. We suggest an emergence criteria (for trapped ACs over depressions) in such simulations, based on the relative length scales of topography and circulation. The lack of bowl-trapped ACs in topographic turbulence theories is discussed. The aforementioned theories only predict strictly steady states. It is possible that the trapped AC is a transient state. However trapped ACs in our bowl simulations are stable over time scales of at least dozens of years. Additionally, it is unclear if local vorticity fluxes, which couple the slope current and AC formation tendencies (section 6), are captured by mean-field approximations in such theories.

The numerical model used here is much too simple to directly apply to the discussed ocean observations of long-lived semi-steady ACs (section 1). One of the potentially important factors which are not included are more complicated stratification conditions (Bashmachnikov et al. 2017). The low stratification conditions, high f, and low planetary β values in the sub-polar areas make this limitation less severe than in other areas. Indeed, Isachsen et al. (2003) found that a barotropic model explains over 50% of seasonal gyre variability in the Nordic Seas (including the Lofoten basin). As mentioned above, each of the observed quasi-stationary vortices has a significant barotropic component (section 5). However, inclusion of surface or bottom mixed layers can lead to submesoscale instability of the eddies (Brannigan et al. 2017). Trapping of near-inertial waves within a fully three dimensional eddy can lead to additional dissipation as well (Fer et al. 2018).

Another limitation is that the neglect of external circulation patterns (e.g., boundary currents and eddy fluxes), and of atmospheric forcing. This limitation is very partially addressed here in the random topography experiments, as different topographic bowls (or bumps) and their emergent circulations, are not isolated from each other. The influence of regional circulation features and perpetual external variability or forcing need to be studied within intermediate complexity models or realistic regional numerical simulations.

Different formation mechanisms were previously suggested and diagnosed for observed semi-stationary ocean ACs (section 1). The present results suggest that whatever the source of low PV material (cf. section 1, e.g., current instability, eddy mergers, deep convection, etc.) and its exact location (cf. section 4) within or near a topographic bowl region, it can lead to bowl-trapped AC formation. A rough estimate of the nonlinearity parameter value in the discussed oceanic basins (section 1) based on bathymetry and observed eddy strengths, gives $\epsilon < 1$, which in our idealized experiments predicts AC formation and topographic trapping. The vertical structure of the formed AC, also in rough agreement with observations, is a reflection of the domain (regionally) averaged vertical structure. As discussed above, in our model, trapped AC formation is related to prograde slope current formation tendency. The tendency for vorticity segregation by eddy fluxes may in principle be tested within more realistic numerical models of the North Atlantic basins.

Acknowledgments. This material is based in part upon work supported by the National Science Foundation under Grant Number OCE-1751386, by the Office of Naval Research (ONR) grant number N00014-18-1-2599, and by the National Aeronautics and Space Administration ROSES Physical Oceanography program under grant number 80NSSC19K1192. This work used the Extreme Science and Engineering Discovery Environment (XSEDE, Towns et al. 2014), which is supported by National Science Foundation grant number ACI-1548562. The SSH altimeter product used is produced by Ssalto/Duacs and distributed by the Copernicus Marine and Environment Monitoring Service (CMEMS) (http://marine.copernicus.eu).

Data availability statement. The AWSIM model code used in this study can be obtained from `https://github.com/andystew7583/AWSIM`.

APPENDIX A

Vortex propagation in homogenized ambient PV over a slope in SWE

Here the motion of an isolated vortex over a slope is examined. Use Reynolds decomposition for any variable, $b = \overline{b} + b'$, the primed terms denoting vortex-induced deviations. PV is denoted by $q = \overline{q} + q'$. A special characteristic examined here is that $\overline{q}$ is constant, i.e., ambient or mean PV is homogenized (as occurs for $0.5 \lesssim \epsilon \lesssim 1$ in our experiments, section 3b). Define the PV-weighted vortex center:

$$X = \frac{1}{Q}\int\int q' x dA, \tag{A1a}$$

$$Y = \frac{1}{Q}\int\int q' y dA, \tag{A1b}$$

$$Q = \int\int q' dA. \tag{A1c}$$

Now,

$$\partial_t X = \frac{1}{Q}\int\int x\partial_t q' dA - \frac{X}{Q}\int\int \partial_t q' dA. \tag{A2}$$

The first integral may be expanded as follows:

$$\int\int x\partial_t q' dA = -\int\int x\mathbf{u}\cdot\nabla q' dA$$
$$= -\int\int \nabla\cdot(x\mathbf{u}q')\,dA + \int\int uq' dA + \int\int xq'\nabla\cdot\mathbf{u}\,dA$$
$$= \int\int uq' dA - \int\int \frac{xq'}{H}\mathbf{u}\cdot\nabla H dA.$$

Here and below boundary terms are assumed to vanish. The velocity divergence term in the last integral was expanded as follows (using that $\nabla\cdot(\mathbf{u}H) = 0$ in SWE):

$$\nabla\cdot\mathbf{u} = \nabla\cdot\left(\frac{\mathbf{u}H}{H}\right) = \frac{1}{H}\nabla\cdot(\mathbf{u}H) - \frac{1}{H}\mathbf{u}\cdot\nabla H = -\frac{1}{H}\mathbf{u}\cdot\nabla H.$$

Similarly, the second integral in (A2) may be expanded as follows:

$$\int\int \partial_t q' dA = -\int\int \mathbf{u}\cdot\nabla q' dA$$
$$= -\int\int \nabla(\mathbf{u}q')\,dA + \int\int q'\nabla\cdot\mathbf{u}\,dA$$
$$= -\int\int \frac{q'}{H}\mathbf{u}\cdot\nabla H dA.$$

Using these expansions within (A2), and defining $x' \equiv x - X$, we finally have

$$\partial_t X = \frac{1}{Q}\int\int uq' dA - \frac{1}{Q}\int\int \frac{x'q'}{H}\mathbf{u}\cdot\nabla H dA. \quad \text{(A3)}$$

Similarly,

$$\partial_t Y = \frac{1}{Q}\int\int vq' dA - \frac{1}{Q}\int\int \frac{y'q'}{H}\mathbf{u}\cdot\nabla H dA. \quad \text{(A4)}$$

The second term in each of the last two equations corresponds to vortex self-propagation, which does not occur in QG approximation (since $\nabla\cdot\mathbf{u} = 0$). It operates by differential self-advection and accompanying relative vorticity stretching over a bottom slope, rather than by planetary vorticity stretching as in topographic beta drift. The latter does not occur here despite of the bottom slope since mean PV is homogenized.

Finally, if the mean flow is along isobaths (say, along the x direction) and if the vortex has an axis of symmetry perpendicular to isobaths, i.e., (v') q' and u' are (anti)symmetric in x', then these symmetries vanish a few of the terms which appeared above, resulting in:

$$\partial_t X = \frac{1}{Q}\int\int \overline{u}q' dA - \frac{1}{Q}\int\int \frac{x'q'}{H}v'\partial_y H dA, \quad \text{(A5)}$$
$$\partial_t Y = 0. \quad \text{(A6)}$$

For an anticyclone the second integral results in a prograde contribution to vortex propagation, i.e., with shallower water to the right. That is, if $\partial_y H < 0$ then $\partial_t X < 0$, since $q' < 0$, $Q < 0$, and $x'v' < 0$.

APPENDIX B

Free linear evolution in a numerical model

To show explicitly that nonlinear effects are critical to the formation of the trapped anticyclone, we conduct a numerical experiment where the nonlinear (advection) terms are not included in the model equations. Since this option was not readily available in the model of Stewart and Dellar (2016), we conducted the linear experiment using the Back of Envelope Ocean Model (BEOM, St-Laurent 2018), a primitive equation layered isopycnal model. Firstly, we ran BEOM in a fully nonlinear configuration identical to experiment $B7E5$, except that BEOM has a free surface rather than rigid upper lid. The BEOM experiment has very similar results to $B7E5$, including a trapped bowl AC and a cyclonic slope current. We conducted a second BEOM experiment identical to the previous, but without the advective terms in the momentum equation. Results are shown in figure B1. The circulation appears, as expected, composed of topographic Rossby waves. No tendency towards AC formation occurred over 1000 days. Indeed, linear dynamics cannot change the azimuthally-averaged azimuthal velocity. That may be seen directly from equation 8a, as the right hand side vanishes under linear dynamics.

References

Arakawa, A., and V. R. Lamb, 1981: A potential enstrophy and energy conserving scheme for the shallow water equations. *Monthly Weather Review*, **109 (1)**, 18–36.

Bashmachnikov, I., M. Sokolovskiy, T. Belonenko, D. Volkov, P. Isachsen, and X. Carton, 2017: On the vertical structure and stability of the Lofoten vortex in the Norwegian Sea. *Deep Sea Research Part I: Oceanographic Research Papers*, **128**, 1–27.

Beckmann, A., and D. Haidvogel, 1997: A numerical simulation of flow at fieberling guyot. *Journal of Geophysical Research: Oceans*, **102 (C3)**, 5595–5613.

Bosse, A., I. Fer, J. M. Lilly, and H. Søiland, 2019: Dynamical controls on the longevity of a non-linear vortex: The case of the lofoten basin eddy. *Scientific reports*, **9 (1)**, 1–13.

Bouchet, F., and A. Venaille, 2012: Statistical mechanics of two-dimensional and geophysical flows. *Physics reports*, **515 (5)**, 227–295.

Brannigan, L., D. P. Marshall, A. C. Naveira Garabato, A. G. Nurser, and J. Kaiser, 2017: Submesoscale instabilities in mesoscale eddies. *J. Phys. Oceanogr*, **47 (12)**, 3061–3085.

Bretherton, F. P., and D. B. Haidvogel, 1976: Two-dimensional turbulence above topography. *J. Fluid Mech.*, **78 (1)**, 129–154.

Brink, K., 1986: Topographic drag due to barotropic flow over the continental shelf and slope. *Journal of physical oceanography*, **16 (12)**, 2150–2158.

Carnevale, G., R. Kloosterziel, and G. Van Heijst, 1991: Propagation of barotropic vortices over topography in a rotating tank. *J. Fluid Mech.*, **233**, 119–139.

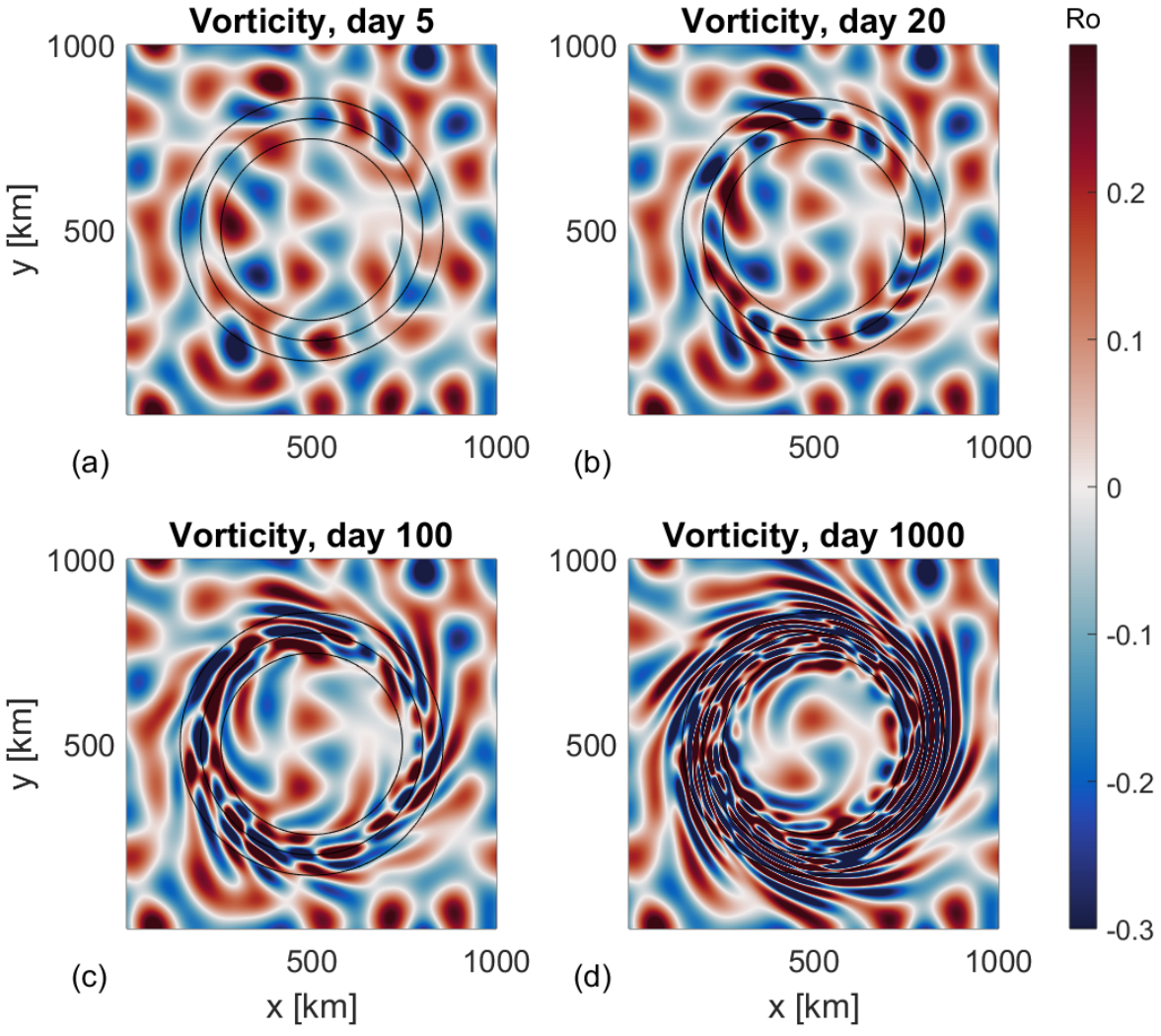

FIG. B14: Linear evolution experiment using BEOM (St-Laurent 2018), with the same topographical parameters and initial conditions as in experiment $B7E5$. Instantaneous vorticity (in f units) distribution is shown at times indicated above each panel. Neither a trapped anticyclone nor a slope current evolve. Motions due to linear topographic Rossby waves are apparent.

Carnevale, G. F., G. K. Vallis, R. Purini, and M. Briscolini, 1988: Propagation of barotropic modons over topography. *Geophysical & Astrophysical Fluid Dynamics*, **41 (1-2)**, 45–101.

Cummins, P. F., and G. Holloway, 1994: On eddy–topographic stress representation. *Journal of physical oceanography*, **24 (3)**, 700–706.

Durran, D. R., 1991: The third-order Adams-Bashforth method: An attractive alternative to leapfrog time differencing. *Mon. Weather Rev.*, **119 (3)**, 702–720.

Fer, I., A. Bosse, B. Ferron, and P. Bouruet-Aubertot, 2018: The dissipation of kinetic energy in the lofoten basin eddy. *Journal of Physical Oceanography*, **48 (6)**, 1299–1316.

Freeland, H., 1994: Ocean circulation at and near cobb seamount. *Deep Sea Research Part I: Oceanographic Research Papers*, **41 (11-12)**, 1715–1732.

Griffies, S. M., and R. W. Hallberg, 2000: Biharmonic friction with a Smagorinsky-like viscosity for use in large-scale eddy-permitting ocean models. *Monthly Weather Review*, **128 (8)**, 2935–2946.

Hogg, N. G., 1973: On the stratified taylor column. *Journal of Fluid Mechanics*, **58 (3)**, 517–537.

Huppert, H. E., and K. Bryan, 1976: Topographically generated eddies. *Deep Sea Research and Oceanographic Abstracts*, Elsevier, Vol. 23, 655–679.

Isachsen, P. E., J. LaCasce, C. Mauritzen, and S. Häkkinen, 2003: Wind-driven variability of the large-scale recirculating flow in the Nordic Seas and Arctic Ocean. *Journal of Physical Oceanography*, **33 (12)**, 2534–2550.

Isern-Fontanet, J., E. García-Ladona, and J. Font, 2006: Vortices of the Mediterranean Sea: An altimetric perspective. *Journal of physical oceanography*, **36 (1)**, 87–103.

Ivanov, Y., and A. Korablev, 1995: Formation and regeneration of the pycnocline lens in the norwegian sea. *Russian Meteorology and Hydrology*, **(9)**, 62–69.

Kloosterziel, R., G. Carnevale, and D. Phillippe, 1993: Propagation of barotropic dipoles over topography in a rotating tank. *Dynamics of atmospheres and oceans*, **19 (1-4)**, 65–100.

Köhl, A., 2007: Generation and stability of a quasi-permanent vortex in the lofoten basin. *J. Phys. Oceanogr*, **37 (11)**, 2637–2651.

Kurganov, A., and E. Tadmor, 2000: New high-resolution central schemes for nonlinear conservation laws and convection–diffusion equations. *Journal of Computational Physics*, **160 (1)**, 241–282.

Le Corre, M., J. Gulaa, A. Smilenovab, and L. Houpertd, 2019: On the dynamics of a deep quasi-permanent anticylonic eddy in the rockall trough. *Association Français de Mécanique, Brest, France, https://cfm2019. sciencesconf. org/245538/document*, 12.

Majda, A., and X. Wang, 2006: *Nonlinear dynamics and statistical theories for basic geophysical flows*. Cambridge University Press.

Mann, C. R., 1967: The termination of the Gulf Stream and the beginning of the North Atlantic Current. *Deep Sea Res. and Oceanographic Abstracts*, **14 (3)**, 337–359.

Marcus, P. S., 1990: Vortex dynamics in a shearing zonal flow. *Journal of Fluid Mechanics*, **215**, 393–430.

Martin, A. P., I. P. Wade, K. J. Richards, and K. J. Heywood, 1998: The PRIME eddy. *Journal of Marine Research*, **56 (2)**, 439–462.

McWilliams, J. C., 2006: *Fundamentals of geophysical fluid dynamics*. Cambridge University Press.

McWilliams, J. C., and G. R. Flierl, 1979: On the evolution of isolated, nonlinear vortices. *J. Phys. Oceanogr*, **9 (6)**, 1155–1182.

Merryfield, W. J., 1998: Effects of stratification on quasi-geostrophic inviscid equilibria. *Journal of Fluid Mechanics*, **354**, 345–356.

Merryfield, W. J., P. F. Cummins, and G. Holloway, 2001: Equilibrium statistical mechanics of barotropic flow over finite topography. *Journal of physical oceanography*, **31 (7)**, 1880–1890.

Nøst, O. A., and P. E. Isachsen, 2003: The large-scale time-mean ocean circulation in the Nordic Seas and Arctic Ocean estimated from simplified dynamics. *Journal of Marine Research*, **61 (2)**, 175–210.

Owens, W. B., and N. G. Hogg, 1980: Oceanic observations of stratified taylor columns near a bump. *Deep Sea Research Part A. Oceanographic Research Papers*, **27 (12)**, 1029–1045.

Pasquero, C., A. Provenzale, and A. Babiano, 2001: Parameterization of dispersion in two-dimensional turbulence. *Journal of Fluid Mechanics*, **439**, 279–303.

Raj, R. P., L. Chafik, J. E. Ø. Nilsen, T. Eldevik, and I. Halo, 2015: The Lofoten Vortex of the Nordic Seas. *Deep Sea Res. Part I: Ocean. Res. Papers*, **96**, 1–14.

Read, J., and R. Pollard, 2001: A long-lived eddy in the Iceland Basin 1998. *Journal of Geophysical Research: Oceans*, **106 (C6)**, 11 411–11 421.

Rhines, P. B., and W. R. Young, 1982: Homogenization of potential vorticity in planetary gyres. *Journal of Fluid Mechanics*, **122**, 347–367.

Richards, C. G., and F. Straneo, 2015: Observations of water mass transformation and eddies in the Lofoten Basin of the Nordic Seas. *Journal of Physical Oceanography*, **45 (6)**, 1735–1756.

Richardson, P. L., 1981: Anticyclonic eddies generated near the corner rise seamounts. *Journal of Marine Research*, **38 (4)**, 673–686.

Rossby, T., 1996: The North Atlantic Current and surrounding waters: At the crossroads. *Rev. Geophys.*, **34 (4)**, 463–481.

Salmon, R., 1998: *Lectures on geophysical fluid dynamics*. Oxford University Press.

Salmon, R., G. Holloway, and M. C. Hendershott, 1976: The equilibrium statistical mechanics of simple quasi-geostrophic models. *J. Fluid Mech.*, **75 (4)**, 691–703.

Shchepetkin, A. F., 1995: Interaction of Turbulent Barotropic Shallow-Water Flow With Topography. *IN THE OCEAN*, 225.

Søiland, H., L. Chafik, and T. Rossby, 2016: On the long-term stability of the lofoten basin eddy. *Journal of Geophysical Research: Oceans*, **121 (7)**, 4438–4449.

Søiland, H., and T. Rossby, 2013: On the structure of the lofoten basin eddy. *Journal of Geophysical Research: Oceans*, **118 (9)**, 4201–4212.

St-Laurent, P., 2018: Back of Envelope Ocean Model (BEOM). Accessed: 2019-12-25, www.nordet.net/beom.html.

Stewart, A. L., and P. J. Dellar, 2016: An energy and potential enstrophy conserving numerical scheme for the multi-layer shallow water equations with complete coriolis force. *Journal of Computational Physics*, **313**, 99–120.

Trodahl, M., P. E. Isachsen, J. Nilsson, J. M. Lilly, and N. Melsom Kristensen, 2020: The regeneration of the Lofoten Vortex through vertical alignment. *Journal of Physical Oceanography*, 1–62.

Tulloch, R., and J. Marshall, 2012: Exploring mechanisms of variability and predictability of Atlantic meridional overturning circulation in two coupled climate models. *Journal of Climate*, **25 (12)**, 4067–4080.

Vallis, G. K., and M. E. Maltrud, 1993: Generation of mean flows and jets on a beta plane and over topography. *Journal of physical oceanography*, **23 (7)**, 1346–1362.

Venaille, A., 2012: Bottom-trapped currents as statistical equilibrium states above topographic anomalies. *J. Fluid Mech.*, **699**, 500–510.

Volkov, D. L., A. A. Kubryakov, and R. Lumpkin, 2015: Formation and variability of the lofoten basin vortex in a high-resolution ocean model. *Deep Sea Research Part I: Oceanographic Research Papers*, **105**, 142–157.

Wade, I. P., and K. J. Heywood, 2001: Tracking the PRIME eddy using satellite altimetry. *Deep Sea Research Part II: Topical Studies in Oceanography*, **48 (4-5)**, 725–737.

White, M., and C. Mohn, 2004: Seamounts: a review of physical processes and their influence on the seamount ecosystem. *OASIS Report contract*, **(38)**.

Willis, J. K., and L.-L. Fu, 2008: Combining altimeter and subsurface float data to estimate the time-averaged circulation in the upper ocean. *Journal of Geophysical Research: Oceans*, **113 (C12)**.

Yu, L.-S., A. Bosse, I. Fer, K. A. Orvik, E. M. Bruvik, I. Hessevik, and K. Kvalsund, 2017: The Lofoten B asin eddy: Three years of evolution as observed by Seagliders. *Journal of Geophysical Research: Oceans*, **122 (8)**, 6814–6834.

Zhao, J., A. Bower, J. Yang, X. Lin, and C. Zhou, 2018: Structure and formation of anticyclonic eddies in the Iceland Basin. *Journal of Geophysical Research: Oceans*, **123 (8)**, 5341–5359.